

Reliability Evaluation of NDT Techniques for Cu-Welds for Risk Assessment of Nuclear Waste Encapsulation

Christina Müller⁽¹⁾, Håkan Rydén⁽²⁾, Mstislav Elagin⁽¹⁾, Carsten Bellon⁽¹⁾, Uwe Ewert⁽¹⁾, Ulf Ronneteg⁽²⁾, Martina Scharmach⁽¹⁾, Bernhard Redmer⁽¹⁾

⁽¹⁾ BAM - Federal Institute for Materials Research and Testing, Unter den Eichen 87; 12205 Berlin; Germany

⁽²⁾ SKB – Svensk Kärnbränslehantering AB; Oskarshamn; Sweden

Keywords

Deposite, Radioactive Waste, Copper Weldings, Risk Assessment, POD Probability of Detection

friction stir welding and electron beam welding. The quality of the welding process and the reliability of the NDT system

Abstract

In order to handle the long living radioactive waste (spent nuclear fuel) SKB is planning to build a deep repository that requires no monitoring by future generations. The spent nuclear fuel will be encapsulated in copper canisters consisting of a graphite cast iron insert shielded by an outer 30-50 mm thick copper cylinder for corrosion protection. The most critical part of the encapsulation process is the sealing of the canister, which is done by welding the copper lid to the cylindrical part of the copper shell using – radiographic and ultrasonic testing - must be satisfactorily determined and combined to derive assumptions regarding the frequency of undetected welding defects for the ensemble of canisters as input for the risk assessment. This is done using the POD method according to the “Reliability Handbook MIL 1823” and its generalization to more complex defect situations in welds.

1 The Swedish Deposit Project



Fig. 1: SKB Canister Laboratory in Oskarshamn

Svensk Kärnbränslehantering AB (SKB, Swedish Nuclear Fuel and Waste Management Co) is responsible for the final disposal of spent nuclear fuel in Sweden.



Fig. 2: Construction Plan of Copper Canisters and the Bedrock Deposit

In order to handle the long living radioactive waste (spent nuclear fuel) SKB is planning to build a deep repository that requires no monitoring by future generations. The spent nuclear fuel will be encapsulated in copper canisters consisting of a graphite cast iron insert shielded by an outer 30-50 mm thick copper cylinder for corrosion protection. The most critical part of the encapsulation process is the sealing of the canister, which is done by welding the copper lid to the cylindrical part of the copper shell. The canisters will then be deposited in the bedrock, embedded in bentonite clay, at a depth of 500 meters.



Fig. 3: Construction of the copper canister

The safety and reliability of the whole systems i.e. the well sealed deposit of the radioactive material under all possible influencing scenarios will be guaranteed by modern means of risk management.

2 Weldings and risk assessment

The welding techniques studied are electron beam welding (EBW) and friction stir welding (FSW). Both techniques are developed in parallel at the SKB Canister Laboratory (see Fig. 1) in Oskarshamn (Sweden) [1]. According to the different metallurgical welding processes they reveal a quite different variety of defects to be detected by NDT techniques and different material micro-structure.

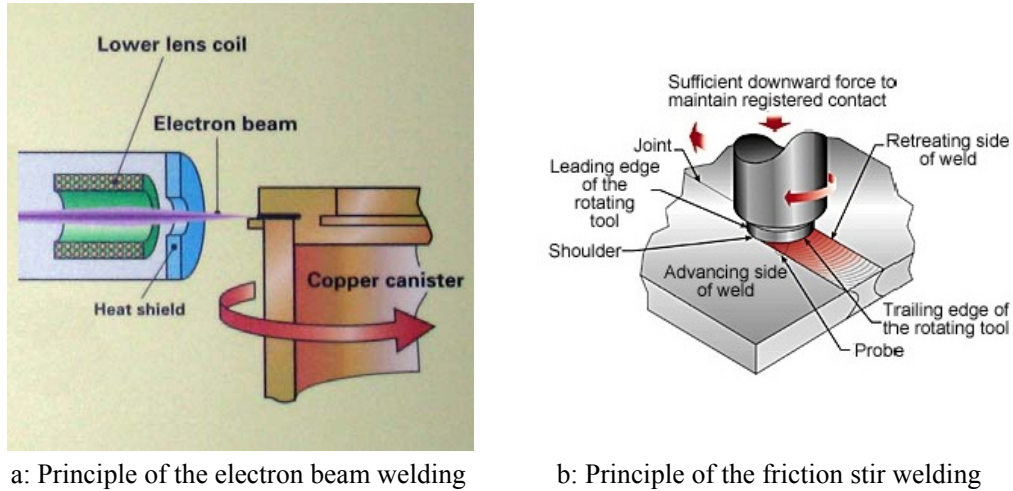


Fig. 4: Principle of the electron beam welding and friction stir welding

A subpart of the final risk assessment of the deep repository construction is to determine the risk of premature canister leak caused by defects in the sealing weld. The defects occurring during the production welding process create a diminishing of the wall thickness. The possible additional reduction of the wall thickness by ground water corrosion makes a minimum rest wall thickness of 15 mm copper necessary. A consequence for the applied NDT methods is to detect all critical defects which would reduce the wall thickness to an amount near or below the 15 mm with a validated high reliability.

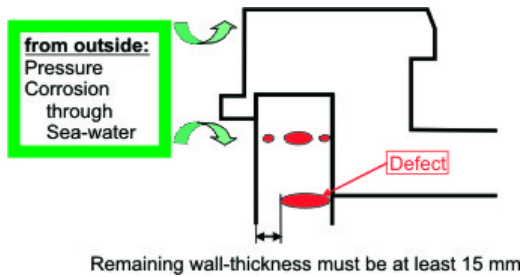
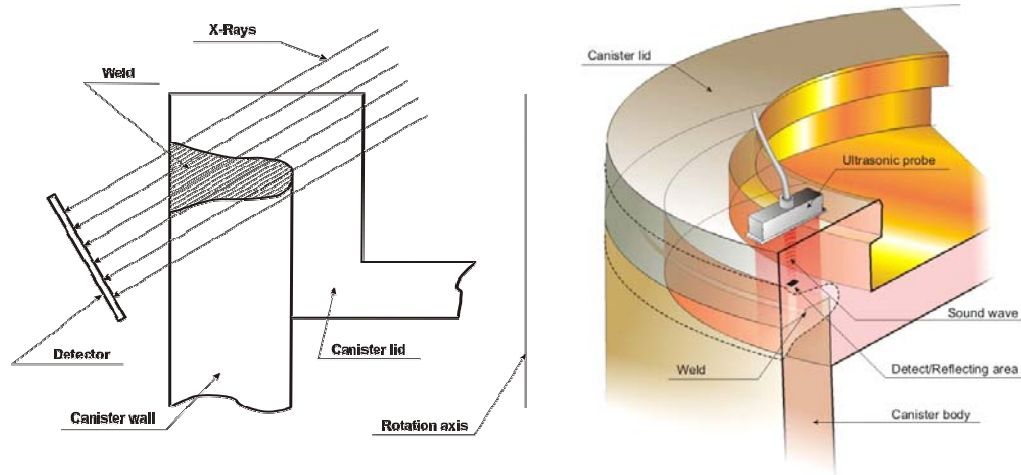


Fig. 5: The weld with possible defect configurations

The NDT techniques applied and adapted by SKB are high energy (9 MeV) X-ray-technique and mechanized ultrasonic phased array technique (2...5 MHz) according to material structure [1].



a: Radiographic testing

b: Mechanized ultrasonic testing with phased array technique

Fig. 6: Non-destructive testing methods used in the project.

The BAM is providing its expertise in optimizing non-destructive testing and in the corresponding reliability assessment to the project. The applied non-destructive testing methods are in a first step checked and optimized concerning the physical parameters and set up according to the latest European and American standards. For the detailed optimization of the radiographic technique the BAM “Xray” simulation tool [2] is applied to various parameter options thus saving lots of expensive experiments.

3 Reliability assessment using POD

Steered by the plan of experiments for the welding procedure optimization and verification, the POD (Probability of Detection) for the defects is determined using a systematic statistical methodology. The POD method, where the detection probability is determined as a function of defect size, was originally developed for the US military aerospace sector [3] for 1-dimensional signals. For the more complex 3-dimensional defect situation in the canister welds and 2-dimensional data fields the method needs to be developed further. From the POD-curve and its lower confidence bound the defect size is derived that will be detected with sufficient reliability and compared to the demand for integrity. This procedure includes series of experiments with the SKB X-ray and ultrasonic methods foreseen for the production.

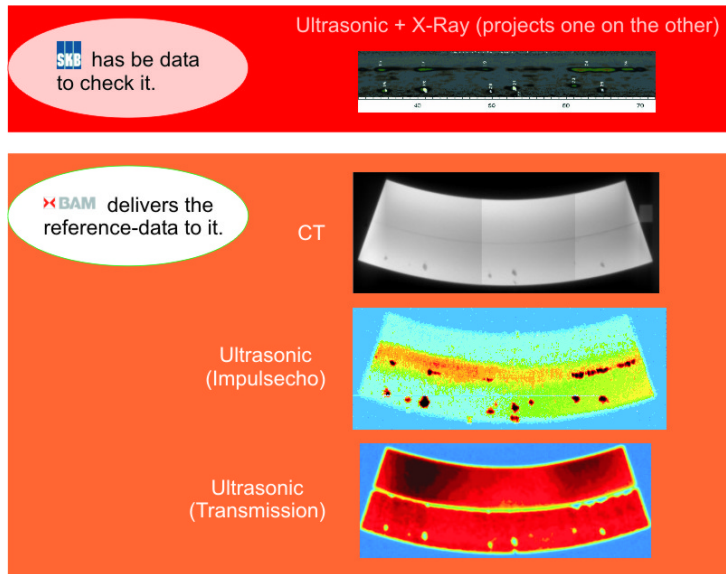


Fig. 7: Example: container L025, section 32-72°

These results have to be compared to true defect configurations in the welds. To determine these “true defect configurations” the welds have to be tested destructively or tested with a more comprehensive non-destructive reference method. To save the parts and the effort for the destruction, the BAM selected a high energy computed tomography (HECT, or CT) method as reference completed by focussed ultrasonic transmission measurement.

The basic principle of the signal response analysis or “ \hat{a} versus a ” evaluation is shown in Fig. 8.

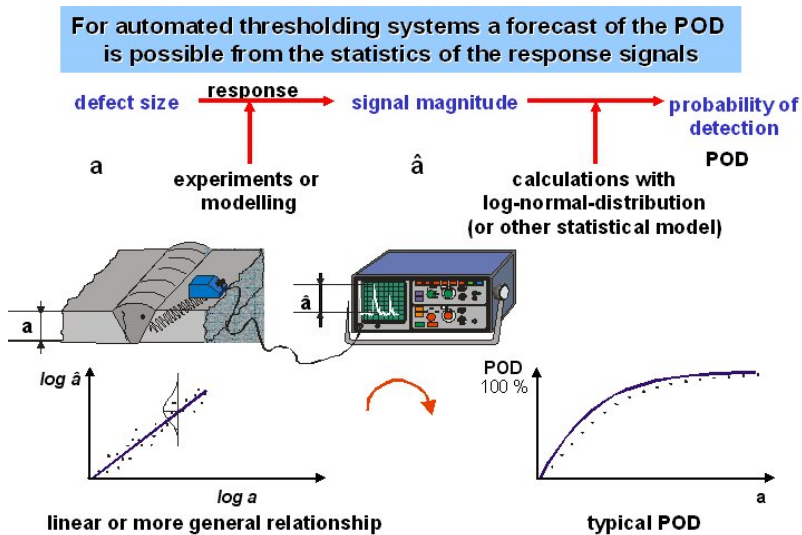


Fig. 8: Quantify the risk: „ \hat{a} versus a “

A defect of size a (crack depth in

Fig. 8) is causing a signal of height \hat{a} . The statistical distribution of the signals in dependence of the defect size yields a certain POD curve which is described in more exact terms in the following section.

3.1 \hat{a} vs. a analysis

General description [4]

Consider a quantitative NDT system. As a result of the investigation of a discontinuity having size a , it generates a signal \hat{a} . If the signal exceeds a certain decision threshold \hat{a}_{dec} , the system registers a flaw detection. As the NDT system is influenced by uncontrolled factors, discontinuities of the same size, can cause signals of different strength. For this reason the strength of the signal \hat{a} to the discontinuity of size a is considered as a random value and associated with a probability density $g_a(\hat{a})$. The relation between a and \hat{a} can be expressed as follows:

$$\hat{a} = \mu(a) + \delta$$

Here $\mu(a)$ equals the mean value of $g_a(\hat{a})$ and δ is the random error whose distribution determines the probability density $g_a(\hat{a})$.

In practice, it is often assumed that δ is distributed normally with zero mean and constant (independent of a) variance. $g_a(\hat{a})$ is then the normal density function with mean $\mu(a)$ and variance equal to that of δ .

The probability of detection (POD) as function of the size of the discontinuity is:

$$POD(a) = P\{\hat{a}(a) > \hat{a}_{dec}\} = \int_{\hat{a}_{dec}}^{+\infty} g_a(\hat{a}) d\hat{a}$$

Fig. 9 illustrates this formula. The probability of detection is represented as hatched part of the area under the bell curve.

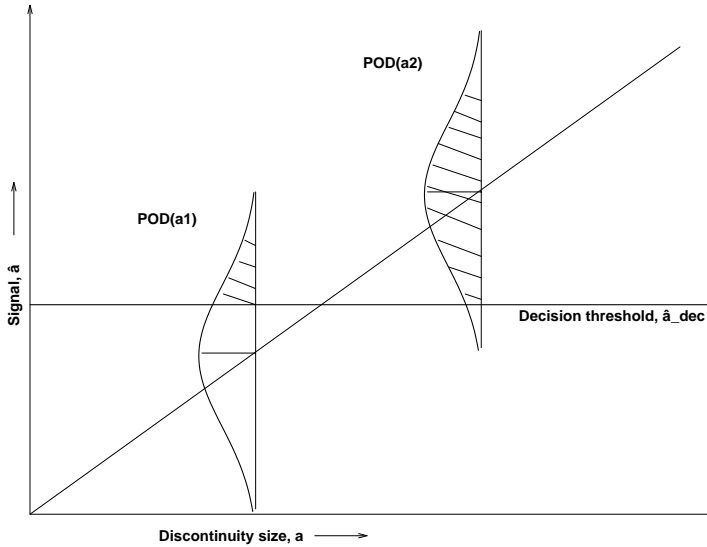


Fig. 9: Probability of detection

Calculation of the POD

Source data are a and \hat{a} – arrays of length n that contain sizes of the defects and response magnitudes, respectively, and the decision threshold \hat{a}_{dec} . Note that the theory for dealing with censored data has been developed (see [4]) but is not used here, because the data sets available to us do not contain censored data. The censored data are the signals that cannot be registered by the system because they are either under the recording threshold or above the saturation threshold.

Calculation of the POD function parameters

The following formula is commonly used to model the relation between a and \hat{a} :

$$\ln \hat{a} = \beta_0 + \beta_1 \ln a + \delta$$

Here δ is normally distributed with zero mean and constant variance σ_δ^2 .

Under the assumptions of the model, the POD function has the following form:

$$POD(a) = P\{\hat{a} > \hat{a}_{dec}\} = P\{\ln(\hat{a}) > \ln(\hat{a}_{dec})\} = \Phi\left(\frac{\ln a - \mu}{\sigma}\right),$$

where Φ is the standard normal distribution function, and

$$\begin{aligned} \mu &= \frac{\ln \hat{a}_{dec} - \beta_0}{\beta_1} \\ \sigma &= \frac{\sigma_\delta}{\beta_1} \end{aligned}$$

The parameters β_0 , β_1 and σ_δ describe the linear dependency of \hat{a} on a and have the following meaning:

β_0	Intercept
β_1	Slope
σ_δ	Standard deviation of the residuals

Their values are estimated from the arrays a and \hat{a} using the method of maximum likelihood.

The 95% lower confidence POD

The 95% lower confidence bound is given by the following formula:

$$\text{POD}_{95}(a) = \Phi(\hat{z} - h)$$

where the variable h reflects the sample size and the scatter of the source data. The calculation of h is thoroughly described in [4].

This general formalism has now to be applied to the defect detection problem within the scope of welding optimization and risk assessment.

3.2 POD - the original task (full program)

The original task (together with the welding optimization) is to make sure that only one of 1000 canisters might contain a critical defect situation where in total more or equal 35 mm of the Cu-wall is missing.

From the naturally real existing POD as a function of all possible influencing parameters we have to extract the POD as function of the flaw radial dimension by a dedicated „Plan of Experiments“ and reasonable mean value operations (see Formula 1). The full program is only feasible with a number of additional experiments until the end of 2005. But in order to learn where we are with our current NDT technique and where to optimize, we need a POD assessment of the state of the art using a “Preliminary POD Assessment”.

$$\text{POD} = f(a_1, \dots, a_n) \rightarrow \text{POD} = g(a_{\text{radial}})$$

Formula 1: Extraction of the POD as a function of the radial size.

3.3 „Preliminary POD assessment“

Volumetric flaws and area-like (non-volumetric) flaws will be treated separately – for EB as well as for FSW

- Volumetric flaws RT
- area like flaws UT

The physically reasonable „ \hat{a} versus a “ POD including physically reasonable 2D extensions will be applied to the parameter configurations shown in the Table 1.

Method	Parameter	Physical meaning
RT	a	penetrated length of a discontinuity
	\hat{a}	maximum contrast
UT	a	area of a discontinuity perpendicular to the sound beam
	\hat{a}	maximum echo height

Table 1. Parameter configurations for the POD calculation.

We determine the $a_{90/95}$ magnitudes i.e. the size a of the flaw for which the lower 95% confidence bound crosses the 90% POD level i.e. it is guaranteed that flaws with a size of $a_{90/95}$ will be detected with 90% probability where only 5% might fall outside this confidence limit in case the experiment is repeated. We work with the assumption – given by the manufacturing experts -- that only one of 100 canisters might have a critical flaw. Then the above argumentation yields: Only one of 1000 canisters might have a leakage.

3.4 Integrity requirement

The flaw radial size has to be limited so that a remaining wall thickness of 15 mm is guaranteed against ground water corrosion. The maximum allowed flaw size in the radial direction is 35 mm. Together with the above POD an additional flaw geometry statistic has to provide for the four groups

- FSW volumetric area-like
- EB volumetric area-like

... separately, no flaws of $a_r \geq 35$ mm will be present. No flaw of radial size $a_r \geq 35$ mm can be among the flaw assembly below $a_{90/95}$, that means no $a \leq a_{90/95}$ should have at the same time an $a_r \geq 35$ mm. This would yield a reasonable justification of the system to meet the above integrity requirement, as long as the existing flaw configurations are representative for the welds. Look for the “correlation” in scatter diagrams:

- penetrated flaw length by X-ray \leftrightarrow radial dimension
- area perpendicular to UT beam \leftrightarrow radial dimension

3.5 Results

Volumetric flaws

In the following diagrams we illustrate the so called preliminary results for the examples of volumetric flaws for EBW and FSW detected by X-rays.

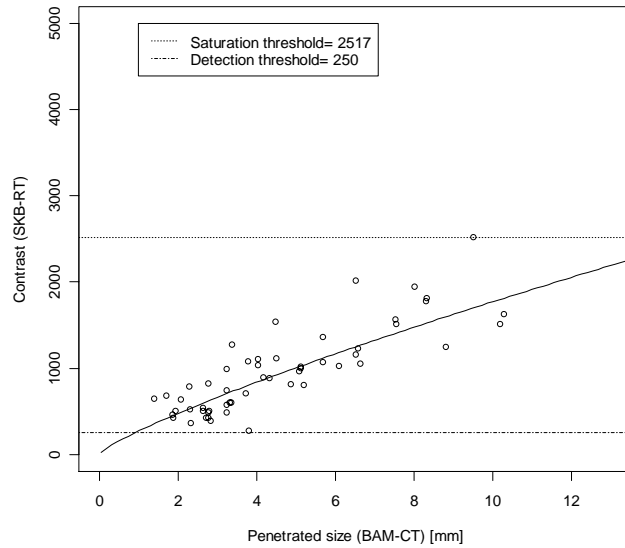


Fig. 10: " \hat{a} vs. a " diagram of the contrast vs. penetrated size (electron beam welding, radiographic inspection, tomographic reference inspection)

Fig. 10 shows the basic " \hat{a} versus a " diagram for the radiographic maximum contrast as a function the defect size penetrated by the X-rays. The dependence is quite linear but shows a considerable scatter.

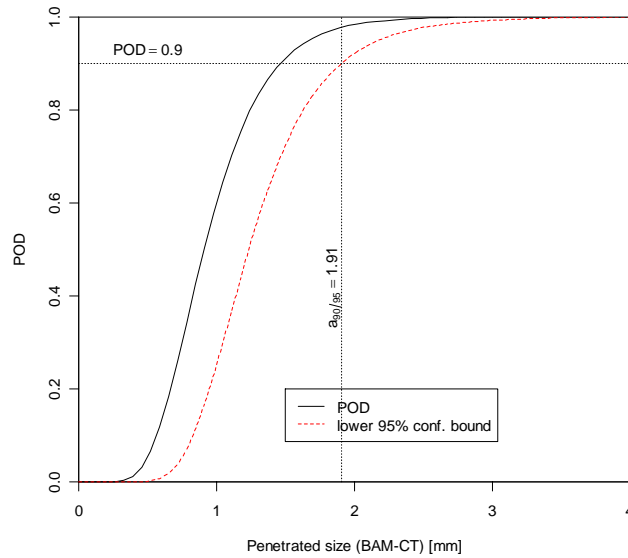


Fig. 11: "Probability of detection" curve (electron beam welding, radiographic inspection, tomographic reference inspection)

The corresponding probability of detection and its lower confidence bound (Fig. 11) yield a $a_{90/95}$ value of about 2 mm for the penetrated size. Now we have to make sure the corresponding radial dimension will not exceed the critical size for all penetrated sizes below $a_{90/95}$.

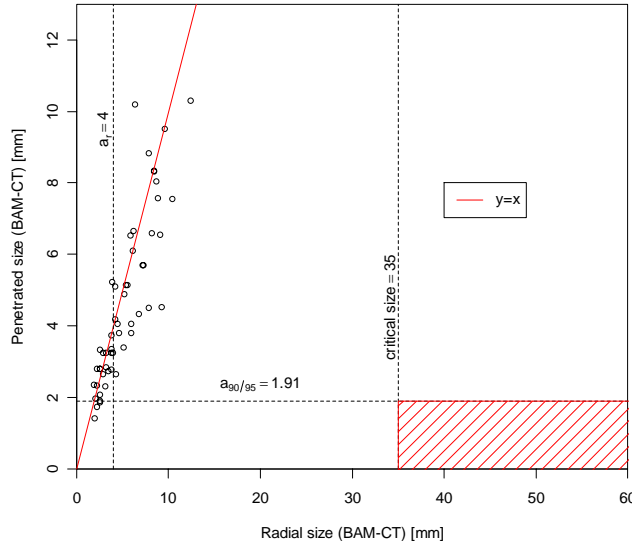


Fig. 12: Scatter diagram of the penetrated size vs. radial size with the critical region (electron beam welding, radiographic inspection, tomographic reference inspection)

Fig. 12 shows the defect size statistics where the penetrated sizes are plotted against the radial dimensions for all observed volumetric flaws for the EBW. The critical region is the red hatched area, where defects with critical radial dimensions above the critical size would occur belonging to sizes a below $a_{90/95}$. As seen in the Fig. 12, the real defect configurations are far away from this.

The Fig. 13 to Fig. 15 show the same types of diagrams for the X-ray investigation of volumetric flaws for FSW. The scatter of signals is wider and the $a_{90/95}$ is a bit bigger. But again all observed defects are far away from the critical region.

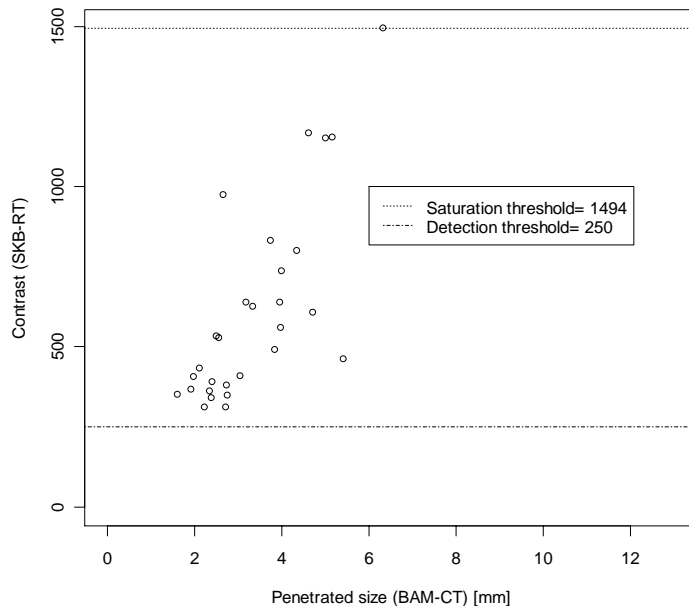


Fig. 13: " \hat{a} vs. a " diagram of the log. contrast vs. penetrated size (friction stir welding, radiographic inspection, tomographic reference inspection)

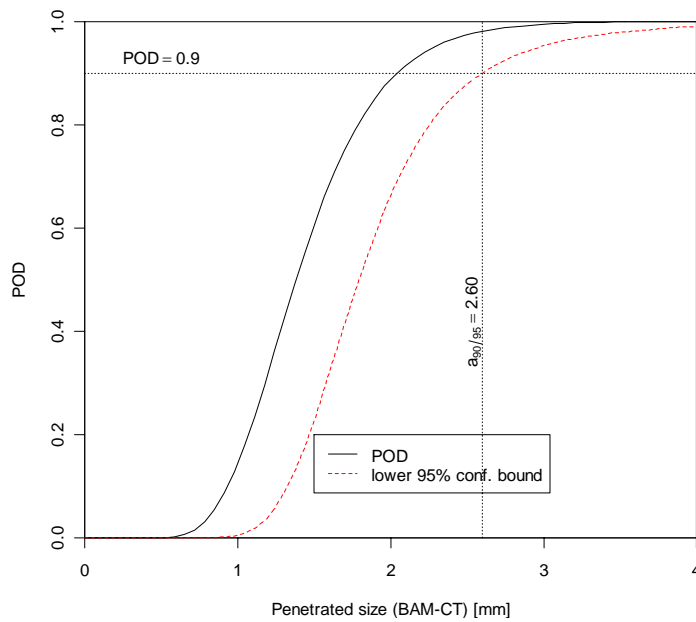


Fig. 14: "Probability of detection" curve (friction stir welding, radiographic inspection, tomographic reference inspection)

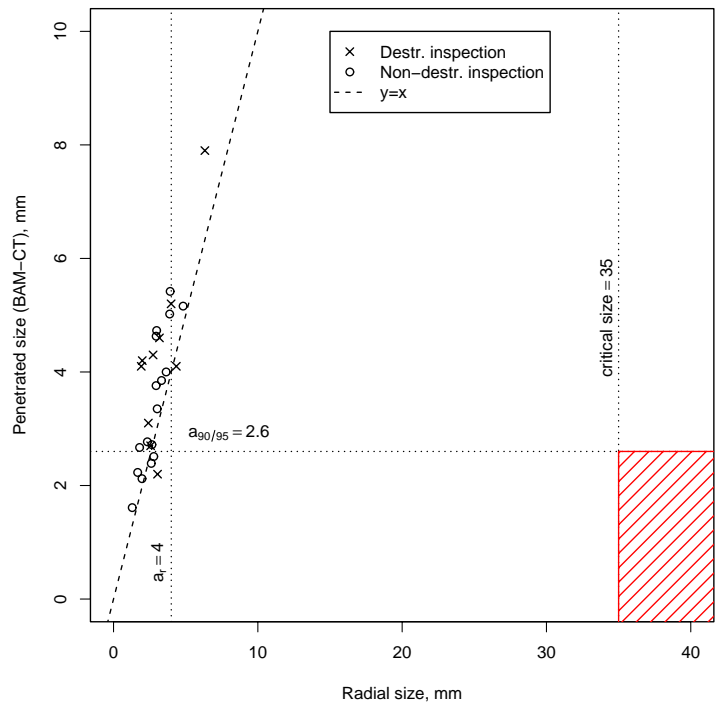


Fig. 15: Scatter diagram of the penetrated size vs. radial size with the critical region (friction stir welding, radiographic inspection, tomographic reference inspection)

Joint line hooking

Another relevant type of flaws occurring in the friction stir welds are the so called joint line hooking (JLH) flaws. An example photo showing the cross section of such a flaw is presented on Fig. 16.

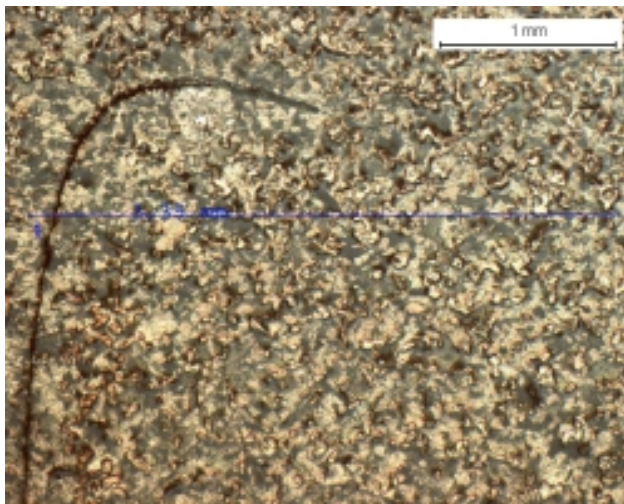


Fig. 16: Cross section of a JLH (Joint Line Hooking)

The first approach in investigating the JLH flaws was to apply the POD method in an empirical way. For \hat{a} we applied the maximum echo amplitude as before. First we created a

totally empirical “ \hat{a} versus a ” scatter diagram (Fig. 17) and POD (Fig. 18) with all the values of the SKB experiments included which yields the $a_{90/95}$ equal to the detectable radial dimension of 4.0 mm based on a threshold of 6% screen height. When we exclude outliers (too small and too big values compared to a "normal" amplitude versus size behavior the detectable radial dimension is 3.2 mm because the scatter is diminished.

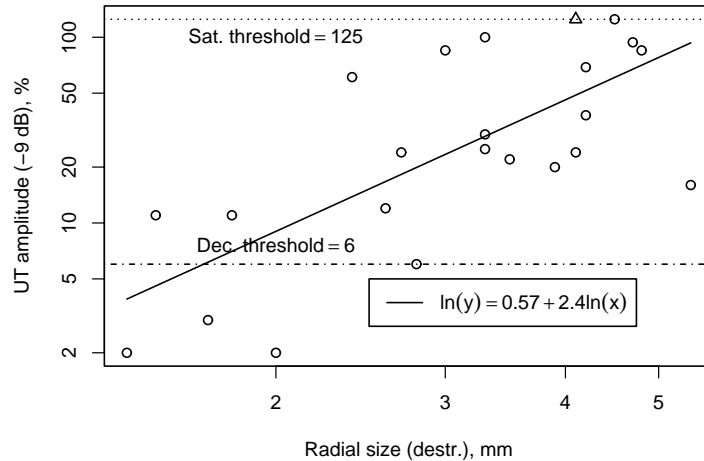


Fig. 17: Scatter diagram of the amplitude vs. radial size for the JLH-type flaws (log. axes).

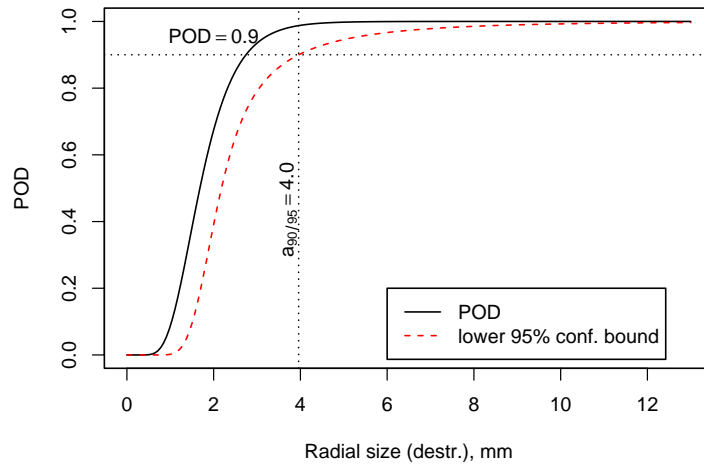


Fig. 18: POD curve for the JLH-type flaws (with outliers).

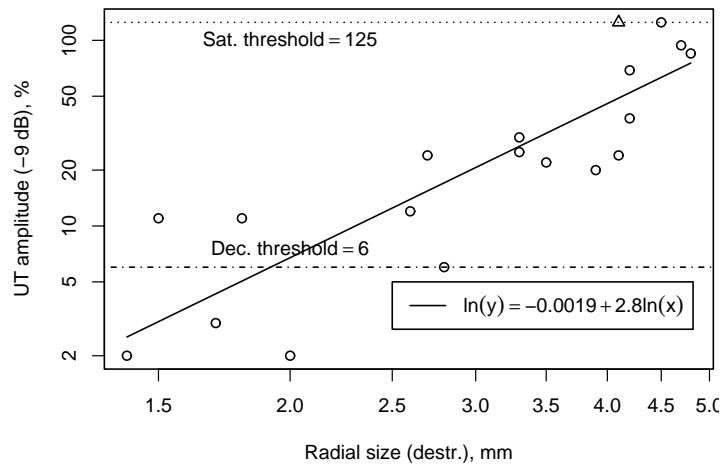


Fig. 19: Scatter diagram of the amplitude vs. radial size for the JLH-type flaws (log. axes, without outliers).

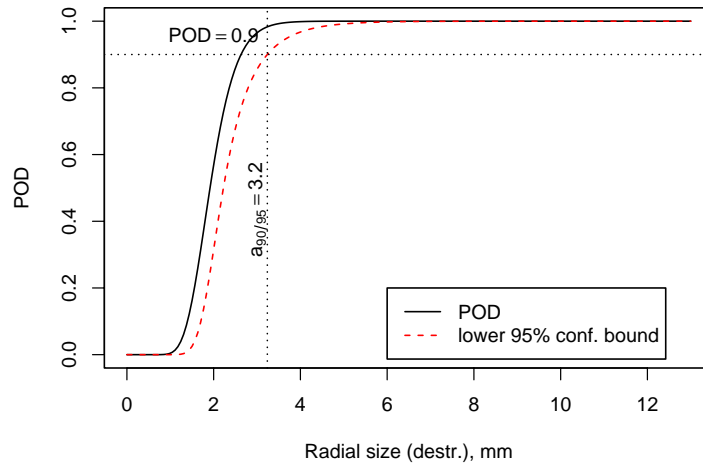


Fig. 20: POD curve for the JLH-type flaws (outliers excluded).

The evaluation of the amplitude data concerning the JLH discontinuities together with the macrographs gave some new information. The reflectivity of the joint line hooking discontinuities (JLH) is not independent from the angle of incidence, as if a side drilled hole were under investigation. This is caused by the geometry of the discontinuity (e.g. radius of curved part, inclination of planar part) and the reflectivity of the discontinuity's surface (e.g. caused by the kissing bond effect). This provides the motivation for separating the whole flaw into regions having different geometrical and reflective properties and being inspected under varying incidence angles. The separation is shown on

Fig. 21.

As the number of data points becomes too small after separation, an UT simulation tool has been used to approximate both experimental situations.

The hook and rectangle parts have been modelled by curved rectangles (sections of cylindrical surface) and flat rectangles, accordingly. Varying curvature radii, radial widths, inclination angles and incidence angles have been considered.

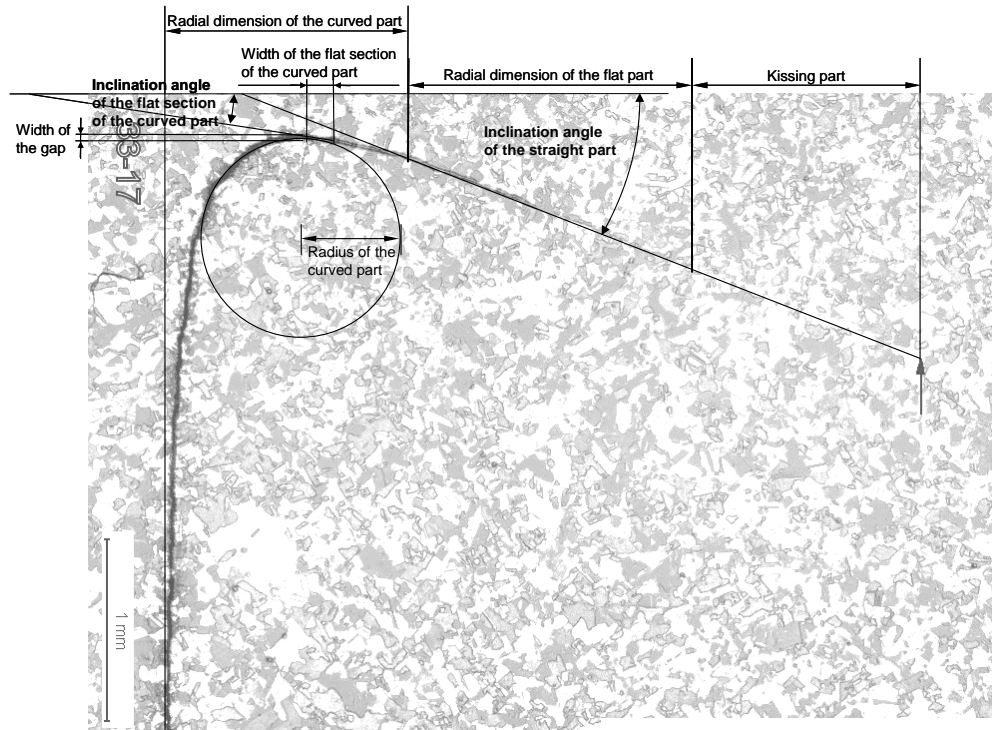


Fig. 21: Regions of the JLH flaws.

An example scatter diagram for a simulated rectangle having the inclination angle of 70 degrees and being inspected under the incidence angle of 20 degrees is shown on **Fig. 22**, and the corresponding POD curve on **Fig. 23**.

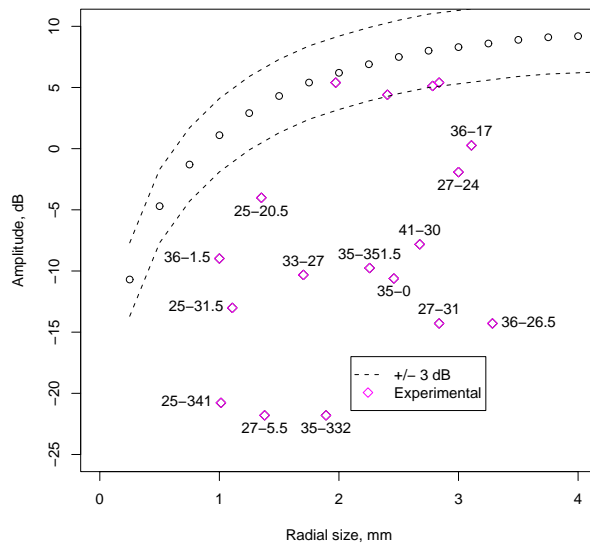


Fig. 22. Simulated scatter diagram (with experimental points representing corresponding parts of real discontinuities) of the amplitude vs. radial size for a simulated rectangle (inclination angle 70 deg., incidence angle 20 deg.).

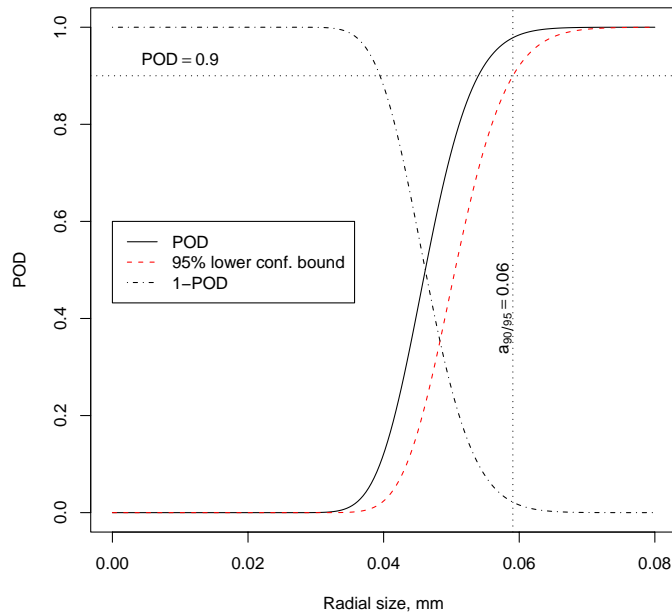


Fig. 23. POD curve based on simulated data for a rectangle (inclination angle 70 deg., incidence angle 20 deg.).

We would like to emphasize here that the modelling background helps to verify that both parts of the JLH are good ultrasonic reflectors, which is confirmed by the model. A greater coincidence between model and experiment can be reached from both sides:

- i) to create a more realistic shaped model in the computer for calculation and
- ii) to create a physical model with the shape closer to the ideal one for template experiments.

Important for the safety consideration is the straight part of the JLH which might grow towards the welding surface. The modelled POD results yield a $a_{90/95}$ below 1 mm which seems to be too optimistic since the modelled echo curve covers the experimental values from the higher side. For further studies it should be analysed systematically what causes the differences in the echo heights.

3.6 Consideration of the total reliability

The PODs considered so far reveal the basic, or intrinsic capability of the NDT methods and do not yet take into account the final industrial application factors and the human factor. The situation for general NDT systems – as outlined in the formula in Formula 2- is described in detail in [5] and [6] and will be applied to the canister welds on a later stage of the project.

$$R \equiv f(IC) - g(AP) - h(HF)$$

Formula 2: Modular approach: the reliability formula

The following table explaining the meaning of the symbols in Formula 2.

R	Total <i>reliability</i> of an NDE system or mine searching system
IC	<i>Intrinsic capability</i> of the system driven by physical laws and technical potential generally considered as an ideal upper bound
AP	The effect of industrial <i>application parameters</i> , such as access restrictions, surface state, generally reducing the capability of the ideal NDE system
HF	The effect of <i>human factors</i> , often further reducing the capability of the NDE system

Result

As result of this SKB-BAM project optimized testing techniques will be provided which are validated for the production process and which will guarantee the required rest wall thickness with sufficient reliability. The joint SKB-BAM project is a contribution for the long term European public safety.

Acknowledgment

The authors like to thank Dr. Gerd_Rüdiger Jaenisch for fruitful scientific discussions and Dr. Jürgen Goebels for providing the reference - CT-measurements on “High energy - CT”. We are also indebted to the colleagues from the ultrasonic group at BAM (Dr. Gerhard Brekow, Dr. Dirk Tschardtke) for ultrasonic reference measurements and Mrs. Sylke Bär for helpful assistance in flaw extraction from data sets.

References

- [1] X. X. RD & D-programme 2001. Technical Report TR-01-30, Svensk Kärnbränslehantering AB, September 2001.
- [2] Gerd-Rüdiger Tillack, Christina Nockemann, and Carsten Bellon. X-ray modelling for industrial applications. *NDT & E International*, 33:481–488, 2000.
- [3] US Department of defense. *Nondestructive evaluation system. Reliability assessment*, 1999. Handbook.
- [4] Alan P. Berens. NDE reliability data analysis. In *Metals Handbook*, volume 17. ASM International, 9 edition, 1989.
- [5] Christina Müller, Thomas Fritz, Gerd-Rüdiger Tillack, Carsten Bellon, and Martina Scharmach. Theory and applications of the modular approach to NDT reliability. *Materials Evaluation*, 59(7):871–874, 2001.
- [6] Christina Müller, Mstislav Elaguine, Martina Scharmach, Bernhard Redmer, Uwe Ewert, Lloyd Schaefer, and Peter-Theodor Wilrich. Reliability investigation of NDE systems by modular analysis of recorded data. In *Proceedings of the 8th European Conference on Non-Destructive Testing*, 2002.

Correspondence Address

Dr. rer. nat., ORRin Christina Müller

postal adress: Bundesanstalt für Materialforschung und – prüfung,
Unter den Eichen 87, 12205 Berlin, Germany

telephone: +49-30 8104 1833

fax number: +49-30 8104 1836

e-mail adress: Christina.Mueller@bam.de

Reliability Tests for Demining

Christina Mueller, Mate Gaal, Mato Pavlovic, Martina Scharmach,

BAM Berlin, Germany

Unter den Eichen 87,

D12205 Berlin, Germany

Christina.Mueller@bam.de

Peter Wilrich FU Berlin, Germany

Abstract

The total detection reliability of a mine searching system is analogous to NDE-systems governed by three elements;

- intrinsic capability - which describes the basic physical-technical capability of the method
- application factors - including those due to environment
- human factor - the effect of human operators on the detection reliability.

Some of these can be determined in simple laboratory measurements in which the effect on detection capability of individual parameters is measured. However, the human factor and some aspects of the effects of environmental conditions on the system need to be treated statistically.

By far the most common "mine searching system" in use today is the metal detector. The test and evaluation procedures for metal detectors described in CEN CWA 14747: 2003 include the above ideas. This is why, in addition to parameter tests, they include detection reliability or blind field tests under local conditions with local personnel.

A series of three field trials was performed in the ITEP-project 2.1.1.2 in 2003 "Reliability Model for Test and Evaluation of Metal Detectors" and another trial named ITEP-project 2.1.1.8 in 2005, in order to specify the optimum conditions to obtain reliable trial results with affordable effort. Each set of specific working conditions is characterized in terms of a combination of one mine type in one soil with one detector handled by local personnel. For each set of conditions, the searching system will deliver a working performance, expressed as mine detection rates as a function of mine depth, and a certain overall false alarm rate. During the ITEP-trials in Benkovac and Oberjettenberg, the authors learned to determine this function separately for each mine type in each soil. This is especially important for low-metal mines in soil that can influence metal detectors, as will be illustrated for the case of the PMA2. Two discussion points remained after 2003; how representative the trials are of field conditions and what is the statistical set-up required if we are to distinguish between the capabilities of individual detectors. In the trials of the ITEP-project 2.1.1.8 a more suitable design of experiment was applied (only two mine types in two soil types on fewer depths). The human factor was considered more carefully in applying some elements of the local SOP (Standard Operating Procedure), thus coming closer to the local practise and field conditions. Until then two detector models had been improved as a result of the previous trials.

Introduction and Background

The CEN Working Group 07 began the process of standardizing test and evaluation methods for Metal Detectors in Humanitarian Demining, including both laboratory measurements of detection capability and blind field trials (reliability tests). In reliability tests, the probability of Detection (POD) and Receiver Operating Characteristics (ROC) curves help to summarize the performance results. Under the umbrella of ITEP (International Test and Evaluation Program for Humanitarian Demining) a number of test trials with metal detectors have been conducted. The aim was to specify the trial set-up and the statistical rules necessary to achieve true, repeatable and reproducible results under representative field conditions. The

trial scenarios ranged from straightforward detection of a large, metallic anti-tank mine, buried near the surface in a soil that does not give metal-detector signals, to the most difficult challenge of detecting low-metal antipersonnel mines, deeply buried in magnetic soil that affects detectors strongly. Individual human factors, such as training and currency of skills were assessed. A full report about the trial conditions and results, including rules for minimum number of targets, operators and numbers of test repetitions necessary to achieve true and reproducible results, have been published on the ITEP website in September 2004 and December 2005.

POD and ROC – Summary of Detection Rates and False Alarms

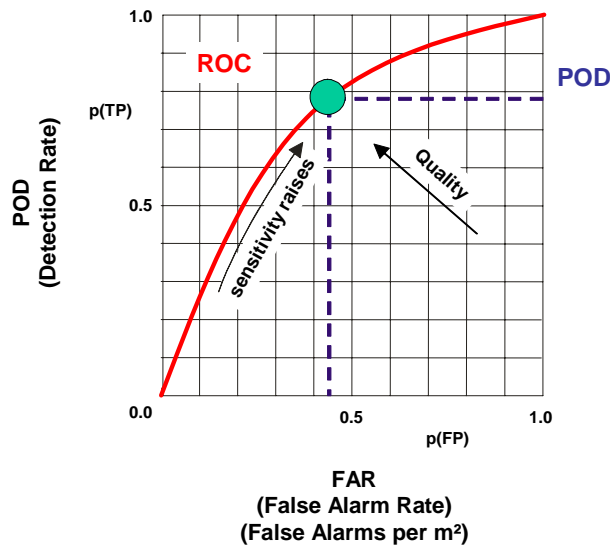


Figure 1: Explanation for ROC and POD diagrams

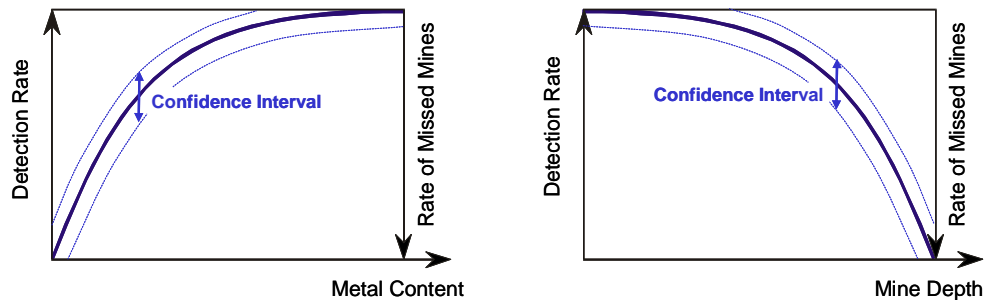


Figure 2: Schematic Representation of POD Curves

The ROC (Receiver Operating Characteristic) of a mine detection system /1/ shows the detection rate or probability of detection versus the false alarm rate or number of false alarms per unit area (Figure 1). The ROC shows how well the system discriminates between signal and noise. The ROC shows how successful the system is in distinguishing between a real signal from a mine and a noise signal arising from any other possible perturbation (from the soil, from other buried artefacts, from the electronics). The closer to the upper left corner the position of a ROC point is, the better is the system.

In the case discussed here, the mine detection systems being tested are metal detectors. Whether detection alarms caused by metal pieces in the ground are considered "true" or "false" detections depends on the aims of the detection reliability trial. An ideal mine detection system would, in principle, be able to distinguish between a mine and a piece of scrap metal. Metal detectors currently used in demining do not have this capability.

For a fixed amount of false alarms the ROC point or operating point of the system for a fixed sensitivity can be taken and further analysed for its dependence on the main influencing factors like the mine depth or the metal content of the mine (Figure 2).



To fit a curve for the dependence of POD on depth, non-linear logistic regression was applied. The POD is transformed according to the following equation and a linear dependence on depth is assumed:

$$\ln\left(\frac{POD}{1-POD}\right) = ax + b,$$

where x is the depth and a and b are parameters of the fit. The parameters a and b are found by Maximum Likelihood.

All these points and curves need to be interpreted in connection with the corresponding confidence bounds to consider the scatter of results. The latter scatter depends on the underlying statistical basis (the number of opportunities to detect the mine) and the natural variability of the factors. The smooth POD or detection rate curves, presented in Figure 2 were determined by the advanced logistic regression model mentioned above/2/. A simple way of obtaining the detection rate curves is by plotting the mean values of the experimentally measured detection rates for each step of burial depth /3, 4, 5, 7/.

Overview about the Parameter Matrix of the Trials

Devices	Soil	Mines	Human Factor
→2 pulse time domain U, X, W →2 continuous wave Y, Z	Types of soil: →Cooperative (neutral) →Uncooperative (Frequency dependent; Constant susceptibility) →Metal contamination of the soil →Homogeneous / heterogeneous	Types of mines: →(metal content): biggest TM  smallest PMA 2  → Depths of mines	→working time →Training mode: →Brief and extended →Status of experience, pre-experience with one device type, age →Current activity →Personal capability
	Trial 2005: → Cooperative (Soil from Sisak) → Homogenous uncooperative, frequency dependent susceptibility (Soil)	PMA1A and PMA2 only	→ Local SOP and System → Quality Assurance → long training → 5 working

from Obrovac)		hours
---------------	--	-------

Figure 3: Test Parameters

The main aim of the trials was to investigate how the device performance manifests itself in different application circumstances. The authors organized three sets of trials in 2003 and another one in 2005 for which the main parameter set up can be seen in Figure 3. The first and third took place in Oberjettenberg WTD 52 on the testing ground of the German Army and the second and the fourth in Benovac, Croatia (CROMAC testing center CTRO).

The conditions for the first trial in May 2003 were representative of poor circumstances, likely to yield low performance: inexperienced operators with a short training period and test lanes with significant metal contamination. Three neutral soils were used and a fourth lane was artificially made "uncooperative" by adding a layer of magnetic blast-furnace slag. (With the benefit of hindsight, we would not recommend this technique because the slag was found to contain metallic particles, creating additional metal contamination). The buried mines were characterized by a large to medium metal content. Some generic "ITOP" targets were also used, irregularly distributed over a predefined depth range.

The second trial set was organized in Benkovac, Croatia with eight experienced Croatian operators, three of whom were active as deminers at the time of the trials. A brief training period (half a day for each detector) was given. There were three types of soil on eight lanes: neutral soil, homogeneous uncooperative soil and heterogeneous uncooperative soil. Both of the latter had frequency-dependent susceptibility. The mines had large, medium or very small metal content and were systematically distributed over a depth ranging between 0 and 20cm to allow statistical analysis. For testing metal detectors the normal target depth should be to the limits of the physical detection capability in the soil. The depth of 20cm was chosen because it is the required depth for mine clearance under Croatian law. The lanes were "almost" clean of metal pieces.

The lessons learnt from first two trials were applied to the third trial set in Oberjettenberg November 2003, with the intention of creating conditions likely to yield better performance. Three new lanes were set up, in addition to the ones available from the previous trial in May, and carefully cleaned of any metal fragments. Mines with large to medium and small metal content were selected and distributed systematically at a depth ranging from 0 to 20cm. The operators, who were inexperienced, were trained carefully in open and blind exercises until they were confident about the reaction of each detector to each mine in each soil and at different depths. To avoid confusion between the different detector operating procedures the operators were assigned during the training, as well as during the first week of the trial, detectors belonging to one class only (double-D coil, static mode or single coil, dynamic mode). In the second week they changed to the other class of detectors.

The new trials in May 2005 (ITEP-project 2.1.1.8) were conducted in Benkovac, Croatia. The same training scheme as in Oberjettenberg November trials was applied, but the training was twice longer. Other improvements were: a reduction to two soil types, two mine types distributed to depths only between 0 cm and 15 cm and the implementation of the working conditions as close as possible to the conditions in minefields (protective equipment, working hours, section leader and quality assurance). Two metal detector models were new in these trials; the manufacturers improved the models used in the last trials based on their results.

Results of the trials

Figure 4 shows the overall results of each trial set, in ROC diagrams. These diagrams illustrate the influence of the factors (Application factor and Human factor) degrading the performance of all the detectors, without distinguishing between individual detectors. The result of inexperienced operators with a short training on metal contaminated ground shows

a mean detection rate of 70% and 0.3 false alarms per m². The artificial uncooperativeness reduces the performance to 60% detection rate and almost one false alarm per m², which is surprisingly poor.

Even more surprising are the total overall results for Benkovac in June 2003, where the operators consisted of eight experienced Croatian deminers. The detection rate of about 65% in neutral soil decreases to almost 50% in a real, local, uncooperative soil with frequency dependent susceptibility. The false alarm rate grows from 0.5 false alarms per m² to almost 0.6. Possible reasons for this extremely poor result are:

- 1) Many of the targets were very deeply buried and in some cases beyond the physical capability of some of the detectors. Minimum metal mines, which are inherently difficult to detect, were buried according to a systematic depth distribution, ranging from 0 to 20cm in order to evaluate the detection rate as a function of depth. The maximum depth of 20cm was chosen because it is the requirement of the Croatian clearance law. A more realistic mean value of detection rate for the region could be determined, if the real depth distribution of mines is known, by using the POD as a function of depth measured in the trial. Usually, AP mines are mainly buried at a depth ranging from 0 to 5cm, which is much shallower than the range used in the trial and would be detected with higher average POD than measured in the trial.
- 2) Only three of the deminers are currently active.
- 3) It has been suggested that experienced deminers may need a longer training phase because they are generally accustomed to using a particular detector model and cannot handle too many different device types at the same time.
- 4) In the trial, the deminers are not in danger and are less motivated to be careful than they would be in a real minefield.
- 5) The test schedule required the deminers to work more quickly and for longer hours than they would normally do.
- 6) The test lanes were contaminated with metal.
- 7) Heterogeneous soil with strong frequency-dependent magnetic susceptibility is a challenge for all detectors, especially in combination with minimum metal mines, since the soil signals often mask the mine signal.

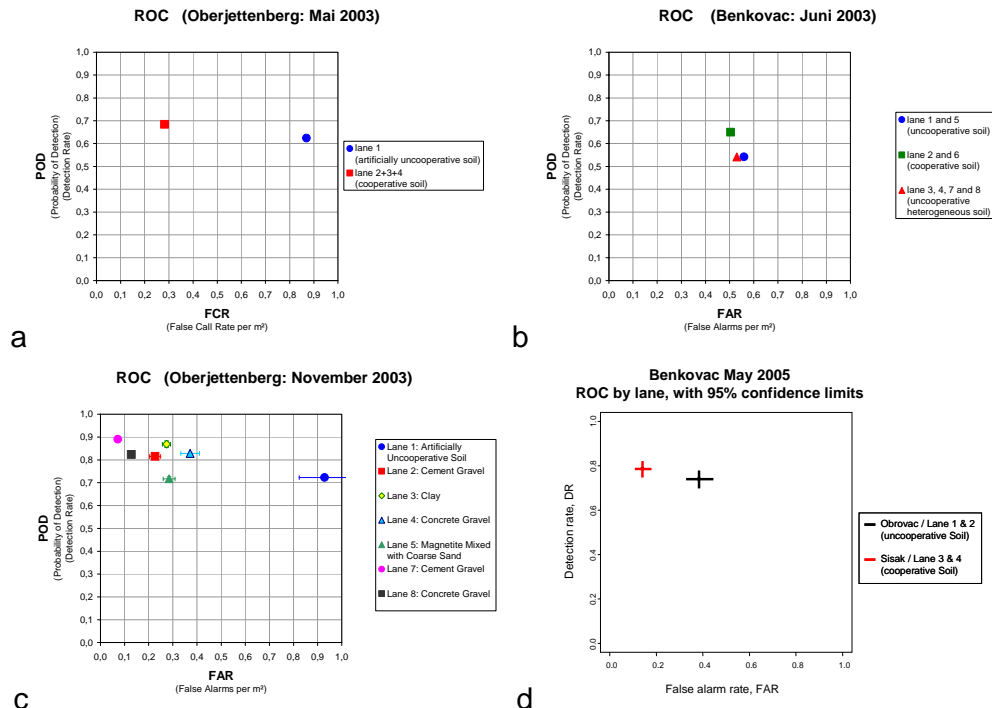


Figure 4: ROC diagrams for different soil and human factor conditions

The performance in the third trial is much better than in the first two, as expected from the conditions of the test with respect to the human factors and application factors. In fig. 4c upper left corner the ROC point is 90% detection rate and false alarms below 0.1 per m². The “secret” is in carefully-conducted and longer training, reduced workload, neutral and very clean soil and targets that are easier to detect. If we want to estimate a realistic POD it is therefore necessary to ask what is the appropriate scenario of application and human factors for the situation we want to investigate. We tried to find the answers to these questions in the trials accomplished in May 2005 again in Benkovac Croatia. This time all 4 deminers were actually working, the training was long and careful like in the November 2003 trial and the local SOP (Standard Operating Procedure) was implemented. The improvements from a) to c) and from b) to d) show how important the proper treatment of the human factor is.

Example of a set of Resulting Curves from Year 2003: Detection Rates as Function of Depth and False Alarms for the PMA2 in different Soils

The following figure gives an overview of soil parameters of all trials 2003.

Soil Types in Oberjettenberg Trials	Ground Reference Height (cm)	Susceptibility at 958 Hz (10 ⁻⁵ SI)	Susceptibility difference at 465 and 4650 Hz (10 ⁻⁵ SI)
Lane 1 artificially uncooperative soil	5 ± 2	244 ± 64	6,1
Lane 2 cement gravel	no signal	0 ± 1	- 0,2
Lane 3 clay	no signal	2 ± 1	- 0,5
Lane 4 concrete gravel	no signal	6 ± 1	- 0,5
Lane 5 magnetite mixed with coarse sand	4,5 ± 0,7	3000 ± 500	6 ± 7
Lane 7 cement gravel	no signal	-1,0 ± 0,2	-0,1 ± 0,2
Lane 8 concrete gravel	no signal	7 ± 1	-0,1 ± 0,1

Soil Types in Benkovac Trials	Ground Reference Height (cm)	Susceptibility at 958 Hz (10 ⁻⁵ SI)	Susceptibility difference at 465 and 4650 Hz (10 ⁻⁵ SI)
Lanes 2, 6 (neutral) Clay from Sisac	no signal	13 ± 2	0,6
Lanes 1, 5 (uncooperative) Laterite soil from Obrovac	18,8 ± 0,9	154 ± 13	25,5
Lanes 3, 4, 7, 8 (uncooperative heterogeneous) local red Bauxite from Bencovac	19,7 ± 2,5	190 ± 36	35,4

Figure 5: Overview of magnetic properties of the soils

In the following Figures the individual detector results are illustrated for the PMA2 minimum metal mine under ideal conditions, i.e. neutral soil without metal contamination, well trained operators and optimized working hours. Figures 6a-d show the detection rates as function of

the burial depth for each device separately and Figure 6e shows the ROC points of all devices together.

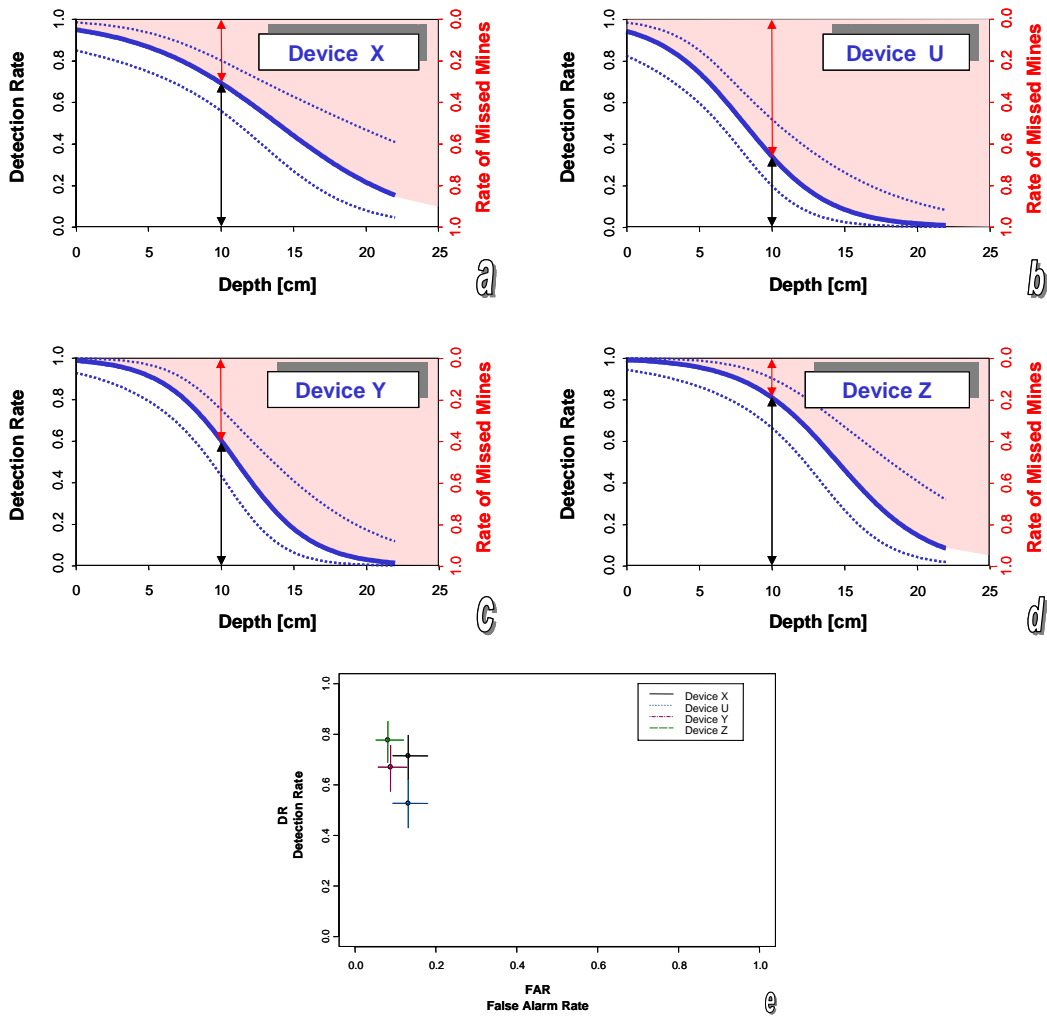


Figure 6: Neutral cooperative soil; only mine PMA-2. Mean value of ROC (detection rate versus false alarm rate) with 95% confidence limits for the different devices

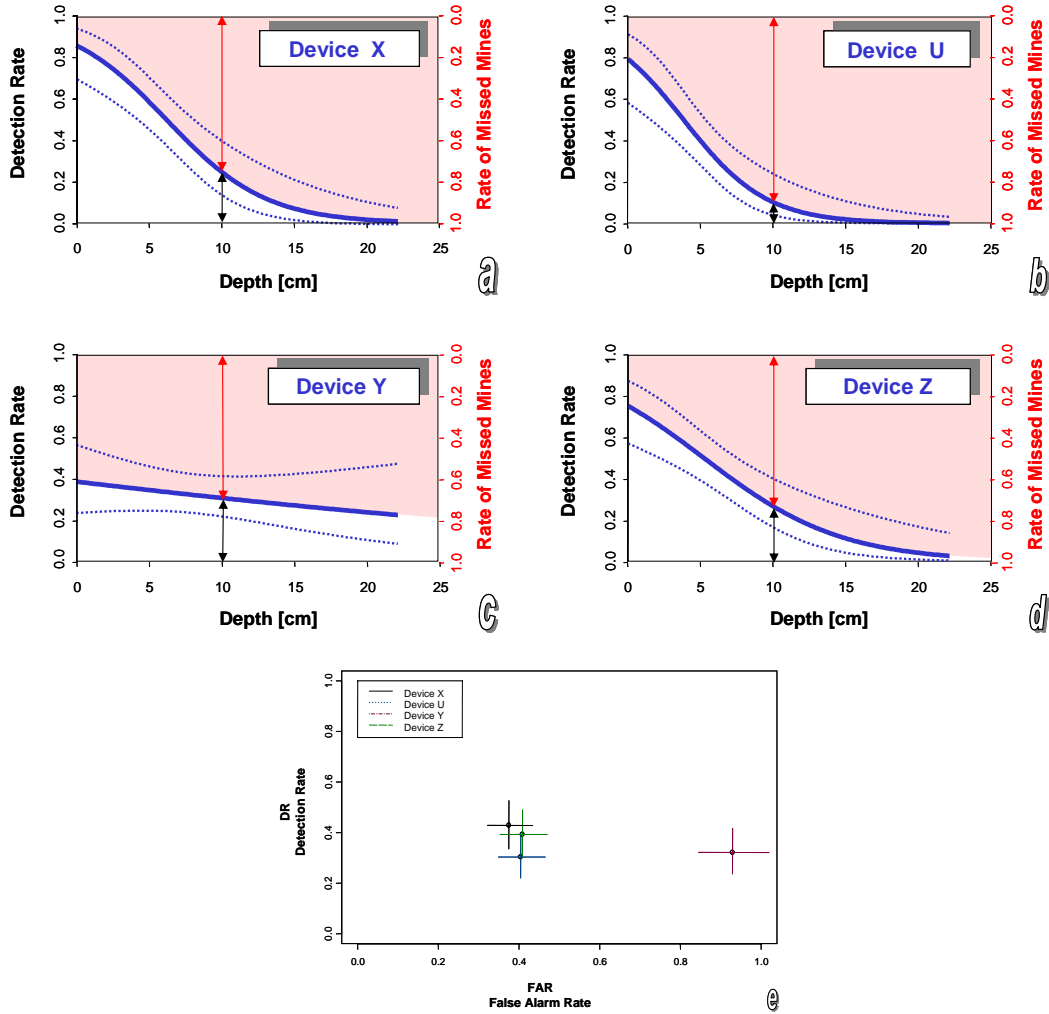
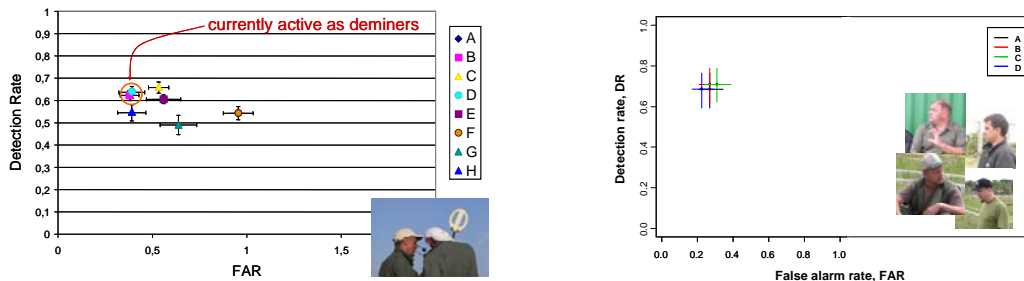


Figure 7: Uncooperative soil, heterogeneous, with frequency dependent susceptibility, red bauxite with neutral stones. Detection rate as function of mine (PMA-2 only) depth for the different four devices with 95% confidence limits



Results of the year 2003

Results of the year 2005, with 95% confidence limits, only PMA-2

Figure 8: ROC-Results for different deminers of the years 2003 and 2005 in Benkovac

Figures 7a-d and Figure 7e present the same results for the most difficult soil. The anomalous result for detector Y is due to a high FAR in the uncooperative soil, up to one

false alarm per m² and the spuriously higher detection rate at large depth. The latter phenomenon can be explained by the fact that some of the “true” positive indications appear to be signals from the soil that happened to fall within the halo of a target, so that the apparent POD does not approach zero at large depth. To avoid this type of anomaly, the soil compensation and sensitivity of the detector should be adjusted to produce an acceptable low FAR prior to starting the blind trial. CWA 14747: 2003 section 8.1.5 specifies a procedure for checking the adjustment of a metal detector to the soil under test. The test is only to be considered valid if the detector can be adjusted in a representative 1m × 1m set-up area so that no false alarms are given when placed on the soil surface and then raised 30mm above it. It seems likely that detector Y was not adjusted (or not adjustable) according to this procedure.

Figure 8 compares the results of each individual deminer in the two trials in Benkovac 2003 and 2005 in ROC diagrams. The lower scatter between their results in 2005 clearly indicate that the human factor influence improved significantly by selecting currently active deminers and providing them adequate training and working conditions according to the local SOP.

Example of a set of Resulting Curves from Year 2005: Detection Rates as Function of Depth and False Alarms for the PMA2 in different Soils

Soil Types in Benkovac Trials	Susceptibility at 958 Hz (10 ⁻⁵ SI)	Susceptibility difference at 465 and 4650 Hz (10 ⁻⁵ SI)
Lanes 1 and 2 (uncooperative)	154 ± 13	25,5
Lanes 3 and 4 (cooperative)	13 ± 2	0,6

Figure 9: Overview of magnetic properties of the soils

In the following figures the individual detector results are illustrated for the PMA2 mine under cooperative conditions for Sisak soil (fig 10a-d): detection rates as function of the PMA2 depth for each device separately and e) the ROC points of all devices together.

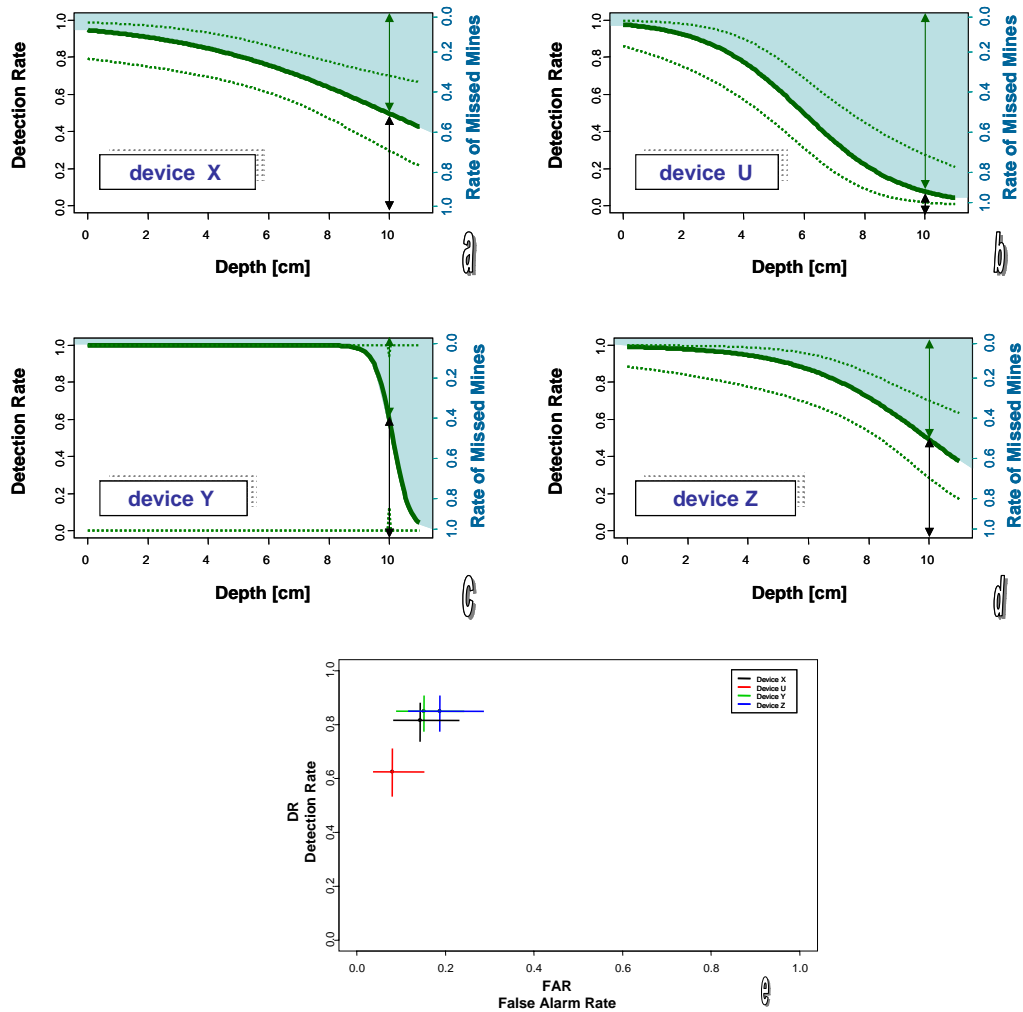


Figure 10: Lanes 3 and 4 (cooperative soil), estimated detection rate with 95% confidence limits for PMA2 – This diagram is comparable with Figure 7

The same curves for each detector but for uncooperative conditions (Obrovac soil) are shown in the figures 11a-e. Especially the comparison of the results for uncooperative soil (fig. 7 – 2003 and fig. 11 – 2005) reveals clearly the improvement by i) better trial conditions and ii) the improvement of the hardware/software of detectors. To make the point i) clearer we put the results of 2003 and 2005 of the identical detectors for the same mines and soils in one diagram in figure 12. This diagram is closer to the realistic detection rates and also indicates more clearly the differences in device performance.

It is the opinion of the authors that the trial procedure with a clear experimental design, careful training and implementation of local working conditions should be added to the existing standard of testing metal detectors CWA 14747:2003, as well as the new insight about maximum detection distance measurements.

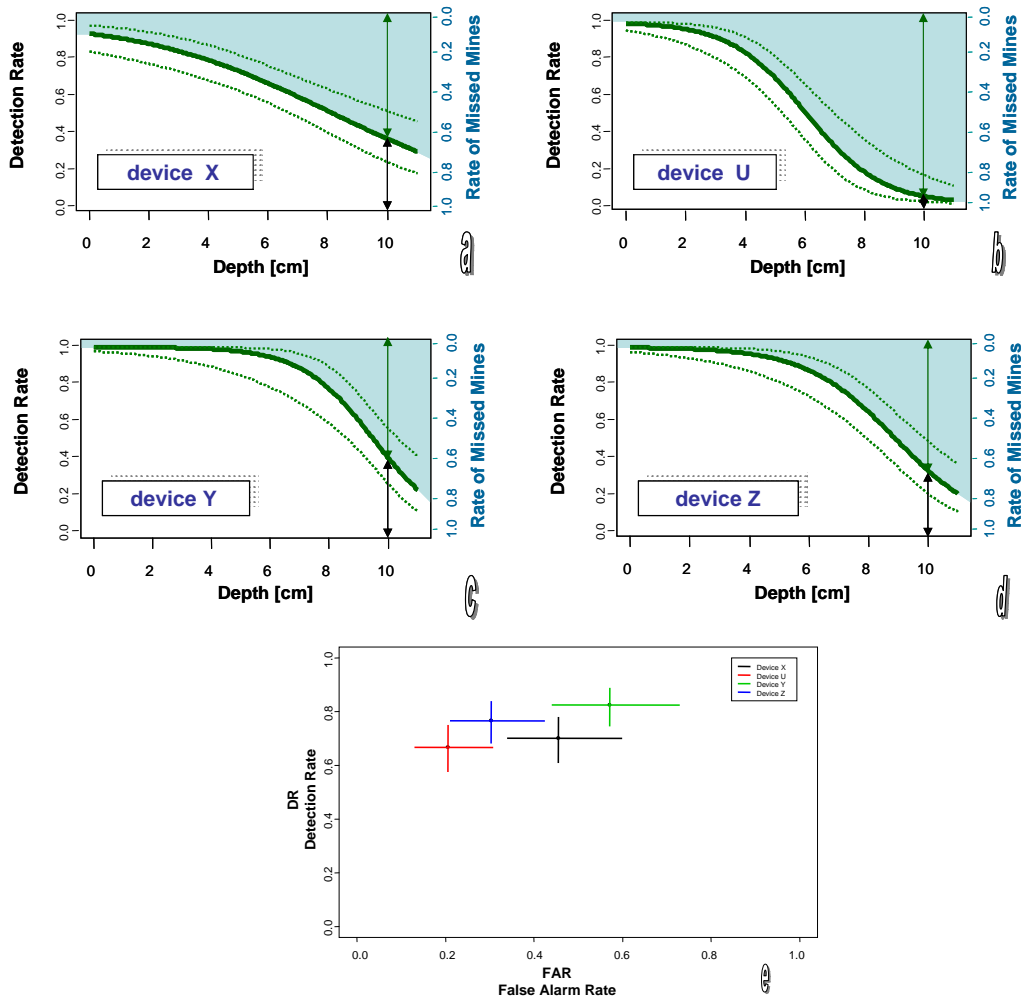


Figure 11: uncooperative soil from Obrovac with a high frequency-dependent magnetic susceptibility; estimated detection rate with 95% confidence limits for PMA2. This soil is very similar to that on Figure 8, though less heterogeneous.

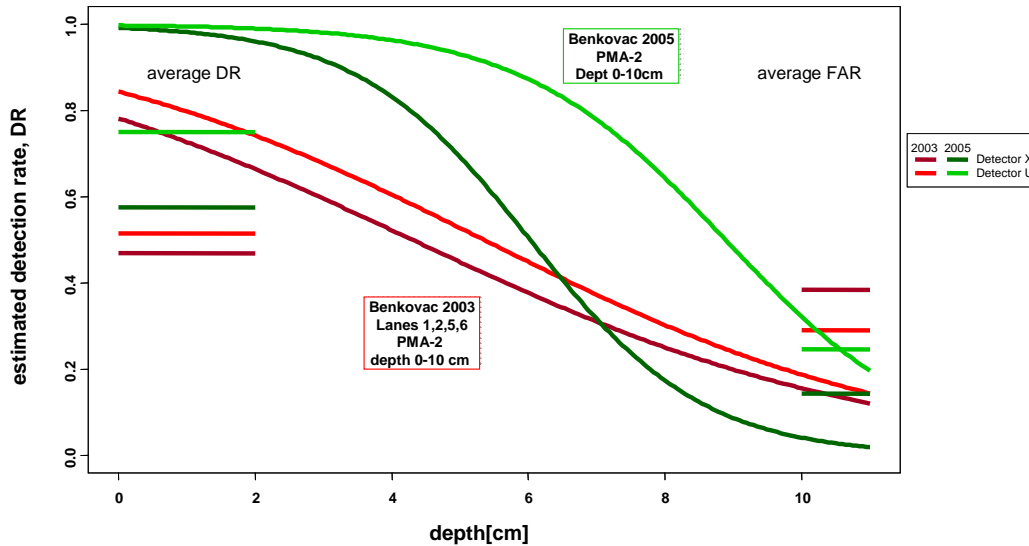


Figure 12: Comparison of individual results of the same detectors (U and X) in Benkovac in the same soils and on the same targets.

Maximum Detection Distance Measurements

For the first time ever (according to our knowledge) the maximum detection distance of a certain combination detector-target was measured several times with different operators (four deminers, twice). The maximum detection distance is the distance between the search head of the metal detector to the top of the target at which the detector starts to give clear signals. The results clearly show that there is a variance in the results that must be taken into account. It seems that the maximum detection distance measurements give results that change within minutes. These changes are not caused only by the operators (deminers), but also by the hardware of the devices.

Figure 13 shows the results for PMA2 in Obrovac soil (lane 1+2) and Sisak soil (Lane 3+4) and in air for PMA2 and PMA1A as mean value and standard deviation of 8 single measurements. The results point to the conclusion that the maximum detection distance measurements should be performed with several operators and repetitions and that the measurements in air can not be considered an indicator of the performance in soil.

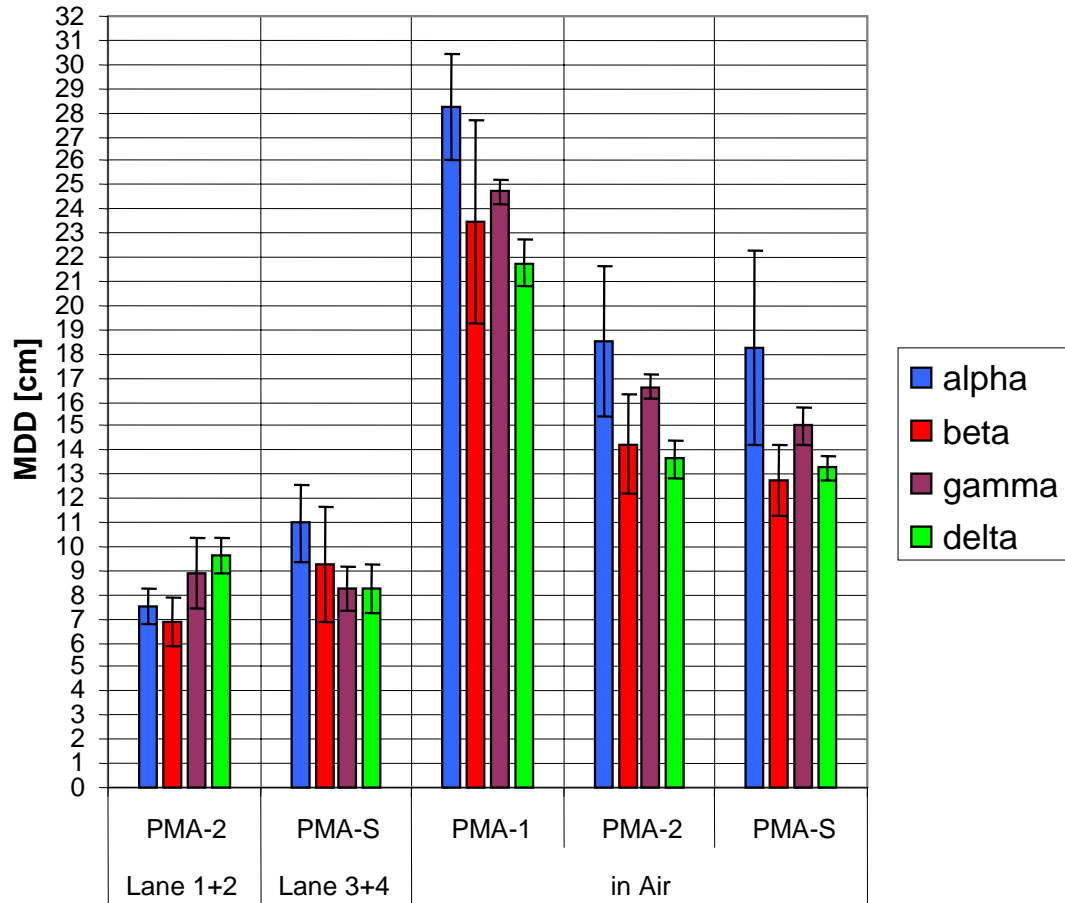


Figure 13: Maximum Detection Distance with the Corresponding Standard Deviations

In addition to the described experiments the trials in 2005 included the investigation of scanned voltage signals on the same test lanes as used for the blind trials. It is the aim of the authors to find a clear relationship between the maximum detection distance and the depth at 50% decrease of the POD from the signal response POD and an assessment of the human factor influence from the comparison of the signal response POD from the scanned results to the POD from blind trials. The results of these attempts will be published in a following paper.

Conclusions and Outlook

For the results of detection reliability field tests the embedding scenario in terms of soil type and cleanness and human factor treatment has to be set up with care and explicit consideration of the local field situation and working system. The characteristics of a detector should be determined in terms of the detection rate as function of depth in each soil for each mine type and completed with the information about the corresponding false alarm rate. An expected mean value of the performance of a detector in a certain region can be determined from these basic curves by superposition, according to the local mine distribution.

Acknowledgment

The authors would like to thank the German Ministry for Foreign Affairs (Lt Col. Detlef Schröder) and the German Ministry of Defence (Lt Col. Manfred Merk) as well as the BAM's presidential Board for sponsorship and support of the project. We are indebted about the fruitful partnership with the CROMAC testing facilities in Benkovac and the WTD 52 in Oberjettenberg as well as We thank for the hands on support of all colleagues from WTD52,

BAM and CROMAC. Especially we thank all the soldiers of the German army and the deminers of Croatia for their brave work.

References

1. Ch. Nockemann, et al., "Performance Demonstration in NDT by Statistical Methods: ROC and POD for Ultrasonic and Radiographic Testing", Proceedings, 6th European Conference on Non Destructive Testing, pp. 37-44 (1994)
2. P.-Th. Wilrich, "Statistical Design of Demining Experiments and Analysis by Logistic Regression", *ITEP Workshop Reliability Tests for Demining*, December, 16-17, 2003 Federal Institute for Materials Research and Testing (BAM) Berlin, 16-17 Dec 2003, Workshop CD or ITEP-ws
3. Ch. Mueller, M. Scharmach, M. Gaal, D. Guelle A. M. Lewis and A. J. Sieber "Performance demonstration for humanitarian demining" *Materialpruefung* Jahrg. 45, Vol. 11-12 pp. 504-512, 2003
4. Ch. Mueller, M. Scharmach, M. Gaal, D. Guelle A. M. Lewis and A. J. Sieber "Proposals for Performance Demonstration and Modular Reliability Assessment for Humanitarian Demining", *International Conference on Requirements and Technologies for the Detection, Removal and Neutralization of Landmine and UXO*, EUDEM2-SCOT, Brussels 15-18 Sep 2003
5. M. Gaal, Ch. Mueller, K. Osterloh, M. Scharmach, S. Baer, U. Ewert, A. M. Lewis, D. Guelle "Metal detector test trials in Germany and Croatia – ITEP Project 2.1.1.2", *MATEST 2003 NDT Achievements and Challenges*, Brijuni-Pula, Croatia 28-30 September 2003
6. Dieter Guelle and Martina Scharmach, ROC-Diagrams for the different lanes, 0312161445-Guelle-14-45.pps on Workshop CD, ITEP-workshop, "Reliability Tests for Demining", 16.-17. December, 2003, Berlin, Germany
7. M. Gaal, S. Baer, T. J. Bloodworth, D. Guelle, A. M. Lewis, Ch. Mueller and M. Scharmach, Optimizing Detector trials for Humanitarian Demining, SPIE, Defense & Security Symposium, April 12-16, 2004, Conference Proceedings

Contact:

Name: Christina Müller
Phone: +49 30 8104 1833
Fax: +49 30 8104 1836
E-mail: Christina.Mueller@bam.de
Address: BAM – VIII.33
Unter den Eichen 87
12205 Berlin
Germany

Regularization approach for inverse problems in order to characterize defects by eddy current NDE

Stéphanie Dubost¹, Yves Goussard², Laurence Châtellier¹, Raphaël Guichard²

¹EDF R&D, 6 quai Watier, 78401 CHATOU CEDEX, FRANCE, ²Biomedical Engineering Institute, Ecole Polytechnique de Montréal, PO Box 6079, Station "Centre Ville", Montréal, Québec, CANADA

Abstract Usual NDE techniques do not produce estimates of the depth of a surface breaking defect when this depth is below 5 mm. We propose a method based on the regularization of inverse problems that allows one to characterize surface breaking defects from eddy current sensors measurements. This method is based on two steps: the first step is the estimation of the characteristics of the inspected medium. The second step is the estimation of the characteristics of the defect. The depth estimates obtained on experimental data are very satisfying.

Keywords – Inverse problems, regularization, eddy current, PSF, reconstruction

1 Introduction

Key power plant components must meet regulatory requirements throughout their lives. Should a defect be detected on a component, plant operators must characterize (e.g. position and evaluate) the defect precisely, and then determine whether the component should be replaced or repaired. Thus, the ability to position and size defects in those major components is a key issue for the life management of plants, from both technical and economical standpoints.

There is nowadays no satisfying NDE technique leading to a correct estimation of the depth of a surface breaking defect when this depth is under 5 mm. The usual technique, which is based on ultrasonic measurements, may indeed be efficient when the defect depth is over 5 mm but does not enable the operator to determine whether the depth is less than 1 mm or between 3 and 5 mm, for example. Such a classification between defects with small depth may however be important to determine the best action to be undertaken in terms of replacement or repair.

In this paper we propose an approach based on eddy current measurement processing, by considering the problem as a so called *inverse problem*. Provided that a defect is present, the aim is to reconstruct a map of material relative conductivity which afterwards enables the operator to estimate several characteristics of the defect, among which its depth.

2 Problem Statement

We consider an austenitic steel object to be inspected with the help of eddy current (EC) sensors. It is assumed that a surface breaking defect is present, that it is isolated from other ones and that its shape is roughly that of a slot or a crack.

An EC sensor is moved on the surface of the component area containing the defect, along lines perpendicular to the direction of the defect length. If no defect is present, the electric field measured by the EC sensor is constant, whereas presence of a defect produces a variation of the electric field. Our goal is to use the set of EC measurements \mathbf{y} to estimate the distribution of relative conductivity \mathbf{x} in the area of interest. The relative conductivity is defined as the ratio $(\sigma - \sigma_0)/\sigma_0$, where σ_0 and σ respectively denote the austenitic steel and defect conductivities. The latter being generally equal to zero, the relative conductivity can be assumed to be either 0 (no defect) or 1 (presence of a defect).

3 Method

3.1 Modeling assumptions

We adopt the three-dimensional (3D), discretized framework schematically depicted in Figure 1. The probe collects measurements close to the surface $k = 0$ of the unknown medium. Our approach is based on a linearized form of the relationship between relative conductivity values \mathbf{x} and measurements \mathbf{y} whose expression is derived using minimal assumptions. More precisely, the linearity of the phenomena implies that the measurements \mathbf{y} can be expressed as the sum of the contributions \mathbf{y}_k ; $1 \leq k \leq K$ of each layer (constant value of index k) of the unknown medium. K denotes the total number of layers. In addition, the medium is assumed to be infinite in the i and j directions; consequently, the phenomena within each layer are shift-invariant and can therefore be expressed as a two-dimensional (2D) convolution product. Using a matrix notation, we can write:

$$\mathbf{y}_k = \mathbf{H}_k \mathbf{x}_k = \mathbf{X}_k \mathbf{h}_k \quad (1)$$

where the components of the 2D point spread function (PSF) which characterizes layer k and the relative conductivity components of layer k are concatenated in vectors \mathbf{h}_k and \mathbf{x}_k , respectively. Matrices \mathbf{H}_k and \mathbf{X}_k are built from the elements of \mathbf{h}_k and \mathbf{x}_k in order to implement a 2D convolution product. From the above equations, we obtain:

$$\mathbf{y} = \sum_{k=1}^K \mathbf{y}_k = \mathbf{H}\mathbf{x} + \mathbf{n} = \mathbf{X}\mathbf{h} + \mathbf{n} \quad (2)$$

where matrices \mathbf{H} and \mathbf{X} and vectors \mathbf{x} and \mathbf{h} are built by appropriate concatenation of quantities \mathbf{H}_k , \mathbf{X}_k , \mathbf{x}_k and \mathbf{h}_k ; $1 \leq k \leq K$, respectively and where \mathbf{n} denotes a noise vector that represents all phenomena not accounted for by the model.

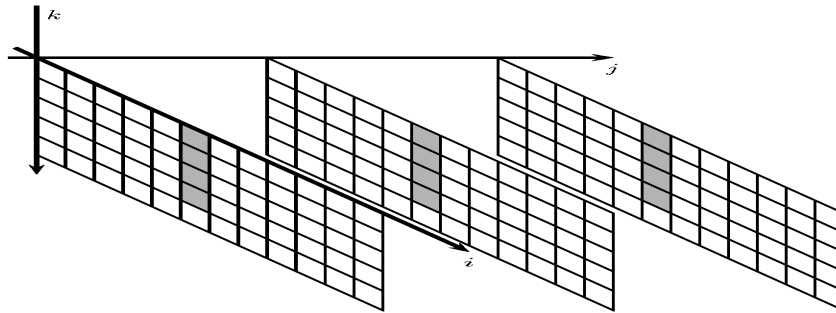


Figure 1 Geometry of the discretized 3D problem. The probe collects measurements close to the surface $k = 0$ of the unknown medium.

3.2 Approach

In the proposed approach, two stages are required: (i) utilization of actual data collected on known defects for estimating the set of PSFs which characterizes the probe/medium response; (ii) estimation of unknown defects using the PSFs obtained at the first stage. At both stages, the estimation problem is ill-conditioned in the sense that the information content and relative size of measured data is rather limited, with the consequence of a high sensitivity of the solutions to observation noise \mathbf{n} [1]. In order to cope with this situation, some form of regularization must be used. Here regularization is achieved by using a *penalized least-squares estimator* at each stage. The penalty term is selected so as to produce an acceptable trade-off between some desirable properties of the estimates and the numerical efficiency of the resulting optimization procedure. These points are detailed in the next two sections.

3.3 PSF Estimation

Due to the nature of the underlying physical phenomena, we assume that each PSF of the set is smooth and that the shapes of the PSFs vary slowly with the depth index k . These characteristics can be encouraged by a quadratic penalty term on, e.g., the gradient of the estimate along the three axis directions. The corresponding penalized least-squares criterion takes the following form:

$$J(\mathbf{h}; \mathbf{y}) = \|\mathbf{y} - \mathbf{Xh}\|^2 + \lambda \|\mathbf{Dh}\|^2 \quad (3)$$

where \mathbf{D} represents the discrete gradient operator (\mathbf{D} is actually the sum of the first difference operators along the three axis directions, with the possible addition of an operator proportional to identity) and where λ is a weighting parameter referred to as the *regularization parameter*. Note that the form $\mathbf{y} = \mathbf{Xh} + \mathbf{n}$ of the model is used at this stage as it is best suited to the estimation of vector \mathbf{h} . Note also that criterion $J(\mathbf{h}; \mathbf{y})$ is quadratic with respect to \mathbf{h} and that the solution can be expressed in closed form. However evaluation of the closed form solution is intractable in practice due to the size of matrices \mathbf{X} and \mathbf{D} . In order to circumvent the difficulty, we chose to minimize $J(\mathbf{h}; \mathbf{y})$ iteratively using a Polak-Ribiere conjugate gradient algorithm whose generic form is given in Table 1 [2]. At this stage, no preconditioning was applied ($\mathbf{M} = \mathbf{I}$). Derivation of the expression of the gradient of $J(\mathbf{h}; \mathbf{y})$ is straightforward from the above equation and the optimal stepsize α (i.e., the stepsize value that produce the maximal decrease of the criterion at each iteration) can also be expressed rather easily in closed form. Finally, the value of regularization parameter λ can be determined either heuristically or using estimation techniques such as generalized cross-validation [3].

$\mathbf{g}^{(n)}$	$= -\nabla J(\mathbf{x}^{(n)})$	
$\mathbf{p}^{(n)}$	$= \mathbf{Mg}^{(n)}$	
$\gamma^{(n)}$	$= \begin{cases} 0 & \text{si } n = 0 \\ \frac{(\mathbf{g}^{(n)} - \mathbf{g}^{(n-1)})^t \mathbf{p}^{(n)}}{(\mathbf{g}^{(n-1)})^t \mathbf{p}^{(n-1)}} & \text{si } n > 0 \end{cases}$	
$\mathbf{d}^{(n)}$	$= \mathbf{p}^{(n)} + \gamma^{(n)} \mathbf{d}^{(n-1)}$	
$\mathbf{x}^{(n+1)}$	$= \mathbf{x}^{(n)} + \alpha^{(n)} \mathbf{d}^{(n)}$	

Table 1 Generic form of the Polak-Ribiere conjugate gradient algorithm used in this study. The quantity to be estimated is denoted by \mathbf{x} . \mathbf{M} , n and α represent the preconditioning matrix, the iteration index and the stepsize, respectively.

3.4 Reconstruction of the unknown medium

The approach to the estimation of \mathbf{x} when the PSFs are known is essentially similar to the one described in the previous paragraph. However, the defects can hardly be considered smooth since they are made up of homogeneous regions separated by sharp discontinuities. In order to account for this characteristic, the penalty term is based upon an *edge-preserving, convex potential function* φ applied to all components and differences between pairs of neighboring components of \mathbf{x} . Function $\varphi(u) = (s^2 + u^2)^{1/2}$, where s represents a scale factor, is essentially similar to the Huber function used in edge-preserving image reconstruction [4]. Therefore, the penalized least-squares criterion used for reconstructing unknown defects takes the following form:

$$J(\mathbf{x}; \mathbf{y}) = \|\mathbf{y} - \mathbf{Hx}\|^2 + \lambda_0 \varphi(\mathbf{x}) + \lambda_1 \varphi(\mathbf{Dx}) \quad (4)$$

where, for any vector \mathbf{v} , the notation $\varphi(\mathbf{v})$ is used in place of $\sum \varphi(v_i)$, the summation being extended to all components of \mathbf{v} . λ_0 and λ_1 denote the regularization parameters and \mathbf{D} represents the same

gradient operator as in the previous paragraph. Note that at this stage, the form $\mathbf{y} = \mathbf{H} \mathbf{x} + \mathbf{n}$ of the model is used because it is best suited to the estimation of \mathbf{x} .

As indicated above, the non-quadratic penalty term in (4) better expresses a salient characteristic of the defects to be reconstructed. Criterion $J(\mathbf{x}; \mathbf{y})$ remains convex and coercive, which guarantees the existence of a unique minimum and is a necessary condition for convergence of iterative descent algorithms toward this unique minimum. However, in general, this convergence is slower than in the quadratic case; in addition, the solution can no longer be expressed in closed form and neither can the stepsize of conjugate gradient techniques.

In order to minimize $J(\mathbf{x}; \mathbf{y})$, we selected the same conjugate gradient algorithm as at the first stage because of its adequate trade-off between numerical efficiency, convergence speed and ease of implementation. In order to speed up the convergence, preconditioning was applied in the form of the inverse of the Hessian of the quadratic term of criterion (4). The gradient can be computed easily, thanks to the simple analytical expression of φ . The stepsize α at each iteration was determined using a simple and fast iterative search [2]. Finally, the regularization parameters were determined in a heuristic manner from the reconstruction of known test defects.

4 Results

4.1 Experimental data

The probe used in our experiments was an air cored coil with a 3.5 mm external diameter used in impedance mode at frequency 300kHz. The acquisition step was equal to 0.2 mm. The experimental data were obtained by inspection of austenitic stainless steel 304L slabs, on which several notches had been electro-eroded. The notches characteristics were: length (15 or 20 mm), width (0.1, 0.2 or 0.3 mm), depth (0.5, 1, 2, 3, 4, 5, 6 mm), and shape (rectangular or semi-elliptical). The discretization step of the medium was equal to 0.2 mm along directions i and j , and to 0.5 mm along direction k . The relative conductivity was estimated up to an 8 mm depth, which corresponds to 16 layers along direction k .

4.2 PSF estimation

4.2.1 Main settings

In a preliminary step, one must *select a data set* from which the PSFs will be estimated. At the PSF estimation stage, the rectangular notches with length 15mm and width 0.2mm were used. As the choice of a data set is not obvious, two data sets leading to two PSF estimates were compared. The first data set contained notches with depths 1, 3, 6 mm, the second one contained notches with depths 0.5, 1, 2, 3, 4, 5, 6 mm. The quality of reconstruction results obtained with the two PSFs was quite identical (slightly better for the first set). This seems to indicate that the data set used must be chosen so that each data provides additional information, which is probably not the case for the second set. The results presented in this paper are obtained with the PSF estimated on the first set.

The *PSF size* must also to be set before performing the estimation. As there was no isolated point defect in the data set, the PSF size could not be assessed by direct observation of the measurements. Selection of the PSF size was performed by making sure that the PSF decreased correctly toward zero at their support boundaries. Another way is to synthesize data from the estimated PSFs corresponding to different sizes, and compare them with the real data. Here, the selected sizes here were 13.4 x 8.2 mm along the i and j directions.

In our experiments, the value of *regularization parameter* λ that appears in (3) was set heuristically by observing the shape of the estimated PSFs: not enough regularization seems to produce “noisy”

estimates whereas too much regularization leads to too “flat” PSFs. Once this physically PSF aspect is accounted for, one can refine parameter values by comparing synthesized data with real ones.

4.2.2 PSF estimation results

An example of PSF estimation result is given in Figure 2. Two PSF layers are shown: left, the PSF corresponding to the first layer (depth between 0 and 0.5 mm), and right the PSF corresponding to the sixth layer (depth between 2.5 and 3 mm).

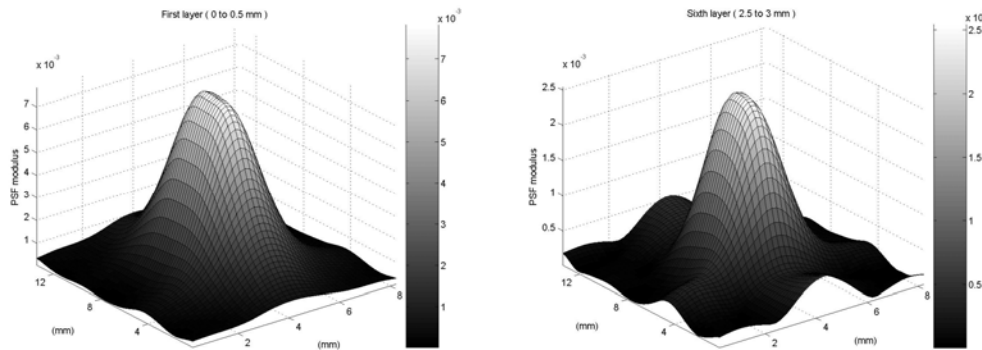


Figure 2 Modulus of the first (left hand side) and sixth (right hand side) layer of the estimated PSF

The estimated PSF have roughly the same shape. Both the magnitude and the support region are larger for layers closer to the surface. We observed that, for deeper layers, the PSF estimates seem to be less regular near the edges.

4.3 Reconstruction of the unknown medium

4.3.1 Main settings

At this stage also, the regularization parameters that appear in (4) must be set before performing the reconstruction. Here too, we used a heuristic approach in which some known defects (in our case: two) were reconstructed for different hyperparameter values. By dichotomy, we choose the parameters that gave the best results in terms of contrast (the reconstruction is as clean as possible) and precision (the estimated characteristics are as close to the real ones as possible). Then, those regularization parameters values were fixed and used for all other reconstructions.

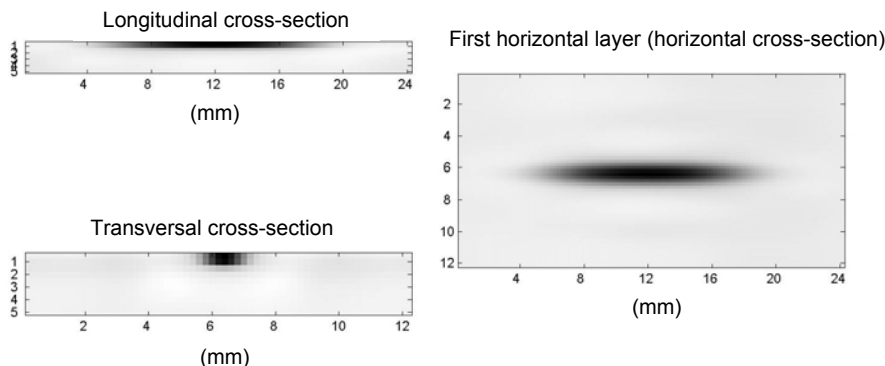


Figure 3 Longitudinal, transversal and horizontal cross-sections of the estimated relative conductivity for the medium containing a rectangular slot with depth 1 mm, length 15 mm, width 0.2 mm

4.3.2 Reconstruction results

The reconstruction results were obtained from data different from the ones used at the PSF estimation stage. An example of reconstruction result is shown in Figure 3. The defect was a rectangular slot with length 15 mm, depth 1 mm, width 0.2 mm (These characteristics are identical to those of a defect used at the PSF estimation stage, but the data were provided by another inspection of the same slab). Three cross-sections are presented (longitudinal, transversal, horizontal) in order to assess the geometry of the defect properly. It can be observed that the reconstruction leads to overestimation of the width, but to satisfactory depth and length estimation.

Additional reconstruction results obtained with 10 other defects are summarized in Table 2. The actual and estimated dimensions of the defects are reported, except for the estimated width which was systematically overestimated (in the order of 0.6 mm).

Shape	rectangular	rectangular	rectangular	rectangular	semi-elliptic	semi-elliptic	rectangular	rectangular	rectangular	rectangular
Depth	1	3	1	3	1	3	1	0.5	3	4
Length	15	15	20	20	15	15	15	15	15	15
Width	0.2	0.2	0.2	0.2	0.2	0.2	0.1	0.2	0.3	0.2
Estimated Depth	~ 1	~ 2.5	~ 1	~ 3	~ 1	~ 2	~ 1.5	~ 1	~ 1.5	~ 3.5
Estimated length	~ 15	~ 15	~ 20	~ 20	~ 10	~ 12	~ 14	~ 14	~ 14	~ 15

Table 2 Reconstruction results for different slots

The following conclusions can be drawn from these and other experiments performed in similar conditions: the *depth* and *length* are correctly estimated for rectangular slots, and slightly underestimated for semi-elliptic slots; the width is systematically overestimated; the shape of the reconstructed defect is not really relevant of the real shape, as it is roughly the same for all defects.

5 Conclusion and perspectives

In this paper we presented a method based on the regularization of inverse problems that provides estimates of the characteristics of unknown defects. The results are satisfying as the main goal, which was to estimate depths defect below 5 mm, seems to be reached at least for rectangular slots.

Some further investigations are in progress in order to improve both methodological and practical aspects. We are indeed working on the improvement of the reconstruction step based on other regularization functions. Practical application of this method to real defects coming from plant components is also in progress.

6 References

- [1] G. Demoment, "Image Reconstruction and Restoration: Overview of Common Estimation Structure and Problems," *IEEE Trans. Acoustics, Speech and Signal Proc.*, vol. ASSP-37, no 12, pp. 2024-2036, 1989.
- [2] J. A. Fessler and S. D. Booth, "Conjugate-Gradient Preconditioning Methods for Shift-Variant PET Image Reconstruction," *IEEE Trans. Image Proc.*, vol. 8, no 5, pp. 688-699, 1999.
- [3] G. H. Golub, M. Heath and G. Wahba. "Generalized Cross-Validation as a Method for Choosing a Good Ridge Parameter," *Technometrics*, vol. 21, no. 2, pp. 215-223, 1979.
- [4] A. H. Delaney and Y. Bresler, "Globally Convergent Edge-Preserving Regularized Reconstruction: An Application to Limited-Angle Tomography," *IEEE Trans. Image Proc.*, vol. 7, no 2, pp. 204-221, 1998.

Possibility of defect detection in multi-layered composite materials used for military applications by IR thermography

by W. Swiderski and D. Szabra

Military Institute of Armament Technology, 7 Prymasa Wyszyńskiego str., Zielonka, 05-220, Poland
E-mail: zak_13@witu.mil.pl

Abstract

Multi-layered composites are used more often in different military applications as constructional materials and light armours protecting against fragments and bullets. Each layer of these materials has very different physical properties. Therefore they are difficult objects to non-destructive testing and making possible detection of subsurface defects of these materials. Typical defects of composite materials are delaminations, lack of adhesives, condensations and crumpling. A method that possibly can be used to non-destructive testing of this type of materials and detection of internal defects deploys infrared thermography. In order to determine the potential use of thermal methods the specialized software was developed for computing 3D (three-dimensional) dynamic temperature distributions in anisotropic six-layered solid body with subsurface defects. In this paper are presented results of simulation representing possibilities for the use of IR thermography methods to test such composite materials.

Keywords: infrared thermography, non-destructive testing, composite material, aramide fabrics, light armours

1. Introduction

The composite materials are applied more and more often to construction of light ballistic protections. In last years the interest with light ballistic protections results from dangers on what troops are exposed participating stabilization-missions. These troops are usually equipped with car vehicles which are exposed against fire from small-calibre weapons and fragments and mines. This demands suitable protection of these vehicles which will assure suitable security level of their crews. In last years the progress in domain of polymers chemistry has made possible the production of materials providing efficient protection against small arms bullets and fragments. Most often composites apply textile materials joined with plastic as such binder creates many-layered composite materials used to personal ballistic protections (vests and helmets for shots and fragments protection) and armours of car vehicles and stationary objects. This type of composite materials are largely made on the basis of very resistant aramid and polyethane fibre joined with phenolic and polyurethane resins and other elastic mixtures. These materials are characterized as light weight, non-corrosive, easy to form what makes them fit well to the surface which they have to protect. These materials can be also applied in connection with steel sheets and ceramics what increases their efficiency on the protection against bullets and fragments. The damaged composite armours can be easily replaced by new ones without disassembling of total protection system.

Defects which can appear in this type of many-layered composite materials usually are inaccuracies in glue of composite layers and stratifications and delaminations occurring under hits of fragments and bullets.

So far used method in resistance testing of light ballistic protections was a destructive testing method called the V50 penetration limit velocity and defined as the velocity when the armour is penetrated at 0,5 probability [1]. Taking into account that light ballistic protections have most often the thickness from several to a dozen or so millimeters and they are made from materials whose thermophysical parameters are decidedly different from parameters of potential defects, which can appear in these materials, leads to a conclusion that an efficient method for non-destructive testing

of these materials may be the IR thermography. Therefore in Military Institute of Armament Technology the work was carried out to examine a possibility for use of IR thermography methods for detection of defects in many-layered composite materials applied in light ballistic protections. A first stage of these works was to work out the software to get effective computer simulations for qualification whether the accepted foundation of testing materials by IR methods is right. Results of analyses received by the new and specialized software which provides 3D modeling of the heat flow in many-layered composite materials are presented in the paper.

2. Mathematical problem

ThermoCalc – 6L™ computer programme [2] developed by V. Vavilov was used to select suitable heating parameters of the composite material tested sample to provide the detection of subsurface defects. ThermoCalc-6L™ software is a further development of the earlier ThermoCalc-3D™ programme. This programme makes possible the investigation of transient phenomena of heat conduction in an object - sample.

Tested object is treated as a solid one placed in the system of Cartesian co-ordinates. In the theoretical model a sample consists of six layers and nine defects and all these elements have shape of parallelepipeds (Fig. 1). The heating or cooling is carried out by applying an external heat impulse on the front surface of the sample. The model assumes that thermal flux on this side is homogeneous or distribution of its density is described by the Gaussian function. In this second case point of maximum flux density may be located in an arbitrary place of heated surface. In general after the stimulated heating or cooling, front and rear surfaces are subjected to a natural cooling process (and in this process also heat exchange exists in the form of convection and radiation) in accordance with the Newton law. For this purpose suitable heat exchange coefficients h are introduced. Thermal parameters of a sample and defects can be defined independently in all three planes of space and this makes possible to characterise it as a fully anisotropic one. The model assumes that side surfaces of sample are constantly isolated adiabatically. However, conditions of temperature continuity and transport of heat flux contribute into the heat transportation process between borders of sample layers as well as between defects and their surroundings. In this model it is assumed to take into account so-called capacitive defects. This is what distinguishes this model from many other practical models in nondestructive testing because in calculations both diffusivity and thermal conductivity of defects are taken into account. Thanks to this it is possible to get the precise description of physical phenomenon in defect and its surroundings.

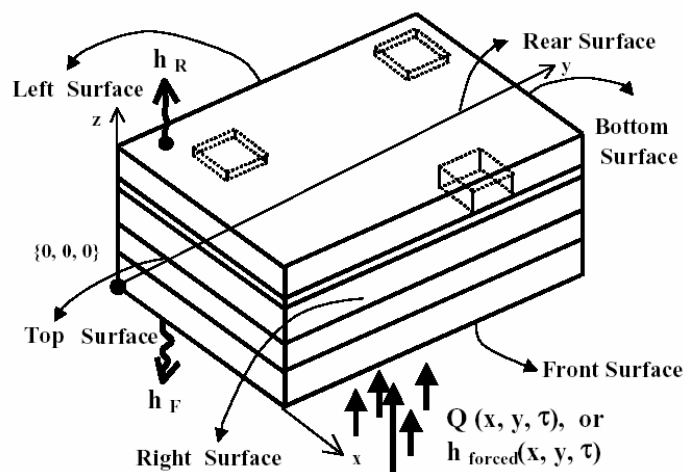


Fig.1. 3D model of sample with subsurface defects

All defects are simulated as parallelepipeds, whose surfaces are properly parallel to surface of border layers and external surfaces of the sample. Defects can be found deep inside layers or appear at point contact with internal border surface whose however they cannot cross. Defects

cannot have point of contact with sample external surfaces neither they can cross these surfaces. According to Fig.1 the sample receives an external thermal stimulus into the front surface.

Transient processes of thermal conductivity in the object (sample) define areas in the three-dimensional system of Cartesian co-ordinates which can be described with following system of equations [2,3]:

- 3D parabolic equation of thermal conduction

$$\frac{\partial T_i(x, y, z, \tau)}{\partial \tau} = \alpha_i^x \cdot \frac{\partial^2 T_i(x, y, z, \tau)}{\partial x^2} + \alpha_i^y \cdot \frac{\partial^2 T_i(x, y, z, \tau)}{\partial y^2} + \alpha_i^z \cdot \frac{\partial^2 T_i(x, y, z, \tau)}{\partial z^2} \quad (1)$$

- initial condition of equation

$$T_i(\tau = 0) = T_{in} \quad (2)$$

- boundary condition for front surface (heating + cooling)

$$-K_1^z \cdot \frac{\partial T_1(x, y, z = 0, \tau)}{\partial z} = Q(x, y, \tau) - h_F \cdot [T_1(x, y, z, \tau) - T_{amb}] \quad (3)$$

- boundary condition for rear surface (cooling only)

$$K_3^z \cdot \frac{\partial T_3(x, y, z = L_z, \tau)}{\partial z} = -h_R \cdot [T_3(x, y, z, \tau) - T_{amb}] \quad (4)$$

- adiabatic conditions on the side surfaces by the coordinates x and y

$$\frac{\partial T_i(x, y, z, \tau)}{\partial x} = 0 \quad \text{for } x = 0, y = 0 \div L_y; x = L_x, y = 0 \div L_y \quad (5)$$

$$\frac{\partial T_i(x, y, z, \tau)}{\partial y} = 0 \quad \text{for } y = 0, x = 0 \div L_x; y = L_y, x = 0 \div L_x$$

- temperature and heat flux continuity conditions on the borders between layers and between layers and defects

$$T_i(x, y, z, \tau) = T_{i\pm 1}(x, y, z, \tau) \quad (6)$$

$$K_i^{q_j} \cdot \frac{\partial T_i(x, y, z, \tau)}{\partial q_j} = K_{i\pm 1}^{q_j} \cdot \frac{\partial T_{i\pm 1}(x, y, z, \tau)}{\partial q_j}$$

Where:

T_i - temperature in the i -th region counted from the initial element temperature ($i = 1 \div 6$ corresponds to sample layers, $i = 7 \div 15$ corresponds to nine defects);

T_{in} - initial temperature of sample;

x, y, z - Cartesian coordinates;

q_j - one of Cartesian coordinates x, y or z ($j = 1 \div 3$);

$\alpha_i^{q_j}$ - thermal diffusivity in the i -th region of the coordinate q_j ;

$K_i^{q_j}$ - thermal conductivity in the i -th region of the coordinate q_j ;

τ - time;

$Q(x, y, \tau)$ - heat flux power density, which generally changes in time and space;

h_F - heat exchange coefficient on the front surface;

h_R - heat exchange coefficient on the rear surface;

T_{amb} - ambient temperature;

L_x, L_y, L_z - sample dimensions.

3. The modelling conditions of thermal diagnostic

3.1. The sample to modellig

In order to evaluate a possibility for the use of IR thermography to detect defects in multilayer composite materials constructed on the basis of polyaramide, the model of a 5 – layer structure was tested by computer ThermoCalc-6L™ program. Computer simulation used two kinds of aramide fabrics. In the first of them fibers were interleaved and arranged perpendicularly to themselves (Fig. 2 a) and in the second one they were arranged in parallel (Fig.2 b).

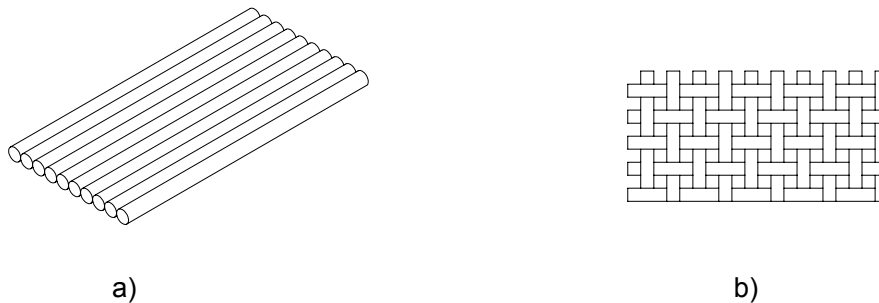


Fig. 2. Structure of polyaramide fabric

Following variants were examined in simulation:

1. Three layers polyaramide (fibres interleaved perpendicularly) thickness 1 mm every joined by formaldehyde resin two layers thickness 0,5 mm every.
2. Three layers polyaramide (fibres parallels) thickness 1 mm every joined by formaldehyde resin two layers thickness 0,5 mm every. In top and bottom layer of polyaramide direction of fibres configuration was the same but in central layer of sample direction of fibres configuration was perpendicular to top and bottom layer of polyaramide.
3. Three layers polyaramide (fibres interleaved perpendicularly) thickness 1 mm every joined by soft rubber layers thickness 0,5 mm every.
4. Three layers polyaramide (fibres parallels so as in variant 2) thickness 1 mm every joined by formaldehyde resin two layers thickness 0,5 mm every.
5. Two layers polyaramide (fibres interleaved perpendicularly) thickness 1 mm every and bottom layer was sheet steel 1 mm thickness every joined by formaldehyde resin two layers thickness 0,5 mm every.
6. Two layers polyaramide (fibres parallels) thickness 1 mm every, layers of polyaramide were oriented in such way that direction of fibres configuration was perpendicular. The bottom layer was sheet steel 1 mm thickness. These layers were joined by formaldehyde resin two layers thickness 0,5 mm every.

The polyaramide is anisotropic and the sample is non-adiabatic.

The thermal properties of the materials are assumed as follows:
 polyaramide – conductivity perpendicular to fibers $\lambda_{\perp} = 0.142 W/(m \cdot K)$; conductivity parallel to fibers $\lambda_{\parallel} = 1.69 W/(m \cdot K)$; density $\rho = 1330 kg/m^3$; heat capacity $C = 1047 J/(kg \cdot K)$; diffusivity perpendicular to fibers $\alpha_{\perp} = 0.1 \cdot 10^{-6} m^2/s$; diffusivity parallel to fibers $\lambda_{\parallel} = 1.19 \cdot 10^{-6} m^2/s$;
 formaldehyde resin - conductivity $\lambda = 0.2 W/(m \cdot K)$; density $\rho = 1200 kg/m^3$; heat capacity $C = 1850 J/(kg \cdot K)$; diffusivity $\alpha = 2.22 \cdot 10^{-6} m^2/s$;
 soft rubber - conductivity $\lambda = 0.13 W/(m \cdot K)$; density $\rho = 1100 kg/m^3$; heat capacity $C = 2010 J/(kg \cdot K)$; diffusivity $\alpha = 0.0588 m^2/s$;
 steel – conductivity $\lambda = 63.9 W/(m \cdot K)$; density $\rho = 7830 kg/m^3$; heat capacity $C = 434 J/(kg \cdot K)$; diffusivity $18.8 m^2/s$;
 air (in thin gaps) - conductivity $\lambda = 0.07 W/(m \cdot K)$; density $\rho = 1.2 kg/m^3$; heat capacity $C = 1005 J/(kg \cdot K)$; diffusivity $\alpha = 5.8 \cdot 10^{-5} m^2/s$.

Defects 1-3 (Fig.3) were located in the first layer of resin (rubber), defects 4-6 were located in the second layer of resin (rubber). Air-filled defects size 5x5 mm had following thicknesses: defects 1 and 4 – 0.1 mm; defects 2 and 5 – 0.2 mm; defects 3 and 6 – 0.5 mm.



Fig. 3. Location of defects in the model of a sample (size 50x100 mm)

The model of a sample was heated on the front surface with a heat pulse. The heating was made with two kinds of square pulses. The first has value power density $Q = 10^5 W/m^2$ and time of heating $\tau_h = 0.1 s$ and for the second value power density $Q = 10^4 W/m^2$ and time of heating $\tau_h = 5 s$.

3.2.Results

One from option of ThermoCalc-6L™ programme calculates the value of a temperature difference (differential temperature signal) between two selected points.

$$\Delta T(\tau) = T[x_1, y_1, \tau] - T[x_2, y_2, \tau] \quad (7)$$

This allows to analyze optimum observation time periods for all introduced defects. These periods depend on defect size and depth. The information concerning the temperature difference between point on the front surface of a sample with being found immediately over a defect and selected point

on the surface outside of the defect and time wherein this difference will be extreme. This is very fundamental for estimation of possibility to use Thermal NDT for testing this type of material. Another Thermal NDT parameter, of whose extremums can be calculated by the Program, is the running temperature contrast:

$$C(\tau) = \Delta T(\tau) / T[x_2, y_2, \tau] \quad (8)$$

In all examined variants defects located in the first layer of resin (rubber) were detected. Only defects in the first layer were detected for the flash heating with power density $Q = 10^5 \text{ W/m}^2$ and time of heating $\tau_h = 0.1 \text{ s}$. For the second value of heating ($Q = 10^4 \text{ W/m}^2$ and $\tau_h = 5 \text{ s}$) defects in second layer of resin (rubber) were also detected. Defect about 0.5 mm thickness was detected in all variants but defect with 0.2 mm thickness was not detected in the 4 variant. Only defect with 0.1 mm thickness (second layer of resin) was not detected in any variants.

Optimum observation time for variant ($Q = 10^5 \text{ W/m}^2$ and $\tau_h = 0.1 \text{ s}$) was from 4.7 s to 6.6 s. For variant ($Q = 10^4 \text{ W/m}^2$ and $\tau_h = 5 \text{ s}$) was from 7.9 s to 10 s (first layer) and from 24 s to 35 s (second layer).

The front surface of sample was heated up to maximum 70°C.

In Table 1 is represented a example of optimum detection parameters for the defects 1-6 (variant 1).

Table 1

Expected detection parameters ($Q = 10^4 \text{ W/m}^2, \tau_h = 5 \text{ s}$ - variant 1)

Defect	$\Delta T, ^\circ\text{C}$	τ_m, s	C, %
1	0.847	8.5	4.9
2	1.457	8.8	6.3
3	2.528	9.5	9.0
4	0.046	24.7	1.1
5	0.109	25.7	2.2
6	0.169	27.8	2.9

4. Conclusion

Results received from computer simulation showed that composite materials consisted of polyaramide are difficult material for nondestructive testing by IR thermography but detection of defects in upper layers of composite is possible. Experimental testing is planned in the future for confirmation of executed computer simulation.

5. Acknowledgments

This work was supported by the State Committee for Scientific Research

REFERENCES

- [1] SWIDERSKI (W.) and HABAJ (W.). – *Thermography – applications to the testing of bullet protection and ballistic limit V50 for composite armours based on reinforced plastics*. Proc. International Conference on Quality Control by Artificial Vision, May 21-23, 2001, Vol.1, p. 49-53
- [2] “ThermoCalc-6L™”, User’s Manual, Tomsk, 2005
- [3] SWIDERSKI (W.). - *Lock-in Thermography to rapid evaluation of destruction area in composite materials used in military applications*, SPIE, Vol. 5132, 2003, pp. 506-517